

Influence of summertime mesoscale convective systems on the heat balance and surface mixed layer dynamics of a large Amazonian hydroelectric reservoir

Marcelo P. Curtarelli¹, Igor Ogashawara², Carlos A. S. Araújo¹, Enner H. Alcântara³, João A. Lorenzzetti¹ and José L. Stech¹

¹ Remote Sensing Division, National Institute for Space Research, São José dos Campos, São Paulo, Brazil.

² Department of Earth Sciences, Indiana University – Purdue University Indianapolis, Indianapolis, IN, USA.

³ Cartography Department, São Paulo State University, Presidente Prudente, São Paulo, Brazil.

Corresponding author: M. P. Curtarelli, Remote Sensing Division, National Institute for Space Research, Avenida dos Astronautas 1.758, 12227-010, São José dos Campos, São Paulo, Brazil
(mpedroso@dsr.inpe.br)

This is the author's manuscript of the article published in final edited form as:

Curtarelli, M. P., Ogashawara, I., Araújo, C. A., Alcântara, E. H., Lorenzzetti, J. A., & Stech, J. L. (2014). Influence of summertime mesoscale convective systems on the heat balance and surface mixed layer dynamics of a large Amazonian hydroelectric reservoir. *Journal of Geophysical Research: Oceans*, 119(12), 8472-8494.
<http://dx.doi.org/10.1002/2014JC010288>

Key points

- We evaluated the impacts of mesoscale systems on an Amazon reservoir dynamics
- Multi-sensor data acquisition was used for the 3D hydrodynamic modeling
- Energy balance and mixing dynamic were affected by the meteorological events

Abstract

We evaluated the impacts of summertime mesoscale convective systems (MCS) on the heat balance and diel surface mixed layer (SML) dynamics of the Brazilian Amazon's Tucuruí Hydroelectric Reservoir (THR). We used a synergistic approach that combines in situ data, remote sensing data and three-dimensional (3D) modeling to investigate the typical behavior of the components of the heat balance and the SML dynamics. During the study period (the austral summer of 2012-2013), 22 days with MCS activity were identified. These events occurred approximately every 4 days, and they were most frequent during January (50% of the observations). An analysis of local meteorological data showed that when MCS occur, the environmental conditions at THR change significantly ($p\text{-value} < 0.01$). The net longwave flux, which was the heat balance component most strongly impacted by MCS, increased more than 32% on days with MCS activity. The daily integrated heat balance became negative (-54 W m^{-2}) on MCS days, while the balance was positive (19 W m^{-2}) on non MCS days. In response to the changes in the heat balance, the SML dynamics changed when a MCS was over the THR. The SML depth was typically 28% higher on the days with MCS ($\sim 1.6 \text{ m}$) compared with the days without MCS ($\sim 1.3 \text{ m}$). The results indicate that MCS are one of the main meteorological disturbances driving the heat balance and the mixing dynamics of Amazonian hydroelectric reservoirs during the summer. These events may have implications for the water quality and greenhouse gas emissions of Amazonian reservoirs.

Index terms: limnology, numerical modeling, mesoscale meteorology, convective process

Key-words: tropical reservoirs, Amazon, mesoscale convective system, heat balance, surface mixed layer dynamics

1. Introduction

Mixing processes play a major role in the ecological dynamics of lakes and reservoirs because of their control over the available nutrients and sunlight that support primary production [Spiegel and Imberger, 1987; Reynolds, 1992; MacIntyre, 2002]. The surface mixed layer (SML) is the portion of the water column immediately below the free surface. The SML is directly influenced by the momentum and turbulence introduced by surface wind stress and buoyancy flux [Imberger, 1985]. The SML thickness varies temporally and spatially, and it is associated with phytoplankton dynamics [Spiegel and Imberger, 1987; Vidal *et al.*, 2010], phosphorus dynamics [Komatsu *et al.*, 2006], cyanobacteria blooms [Atoui *et al.*, 2012] and greenhouse gas emissions [Eugster *et al.* 2003; Rudorff *et al.*, 2011]. The SML dynamics in lakes and reservoirs worldwide are well documented in the available literature [Imberger, 1985; Spiegel and Imberger, 1987; MacIntyre *et al.* 2002; Curtarelli *et al.* 2014]. However, research is lacking for Amazonian lakes and reservoirs, where a better understanding of the spatio-temporal variations in the SML thickness and associated forcing is still needed.

For tropical and equatorial lakes and reservoirs, MacIntyre *et al.* [2002] showed that at the diel scale, the upper water column is stratified during the day and is nearly isothermal at night. The diel dynamics of the SML are mostly modulated by the surface energy balance, which in turn is modulated by meteorological conditions and atmospheric boundary layer (ABL) stability [Verburg and Antenucci, 2010]. Thus, short-duration meteorological events, such as mesoscale convective systems (MCS), that are frequently observed in the region can affect SML dynamics in Amazonia aquatic systems by influencing the cloud cover formation and weather conditions [Laurent *et al.*, 2002; Houze, 2004; Tadesse and Anagnostou, 2010].

The Amazon region is known as one of the largest lakes district in the world [Sippel *et al.* 1992], and it is one of the main centers of convective activity in the tropics [Laurent *et al.*, 2002].

In this region, MCS activity occurs throughout the year, but it is most frequent during the wet season (austral summer) when the South Atlantic Convergence Zone (SACZ) and the Inter-Tropical Convergence Zone (ITCZ) are present [*Liebman et al.*, 1999]. These events generally occur at intervals from 8 to 10 days [*Nogués-Paegle and Mo*, 1997]. Thermodynamic instability and the low-level vertical shear of the horizontal wind control the organization and propagation of MCS [*Machado*, 2000; *Laurent et al.*, 2002].

Considering that MCS affect surface winds, air temperature, and cloud cover and decrease the incident shortwave radiation, this study aimed to evaluate the impacts of MCS activity on the heat balance and SML dynamics of a large hydroelectric reservoir located in the Brazilian Amazon during the austral summer. A combined approach – in situ data, remote sensing and three-dimensional (3D) hydrodynamic modeling – was used to avoid the limitations of a one-dimensional approach in understanding vertical mixing and transport through the thermocline [*MacIntyre et al.* 2002]

A summary of the environmental characteristics of the study site is presented in section 2. The methodology of the research is described in section 3. Subsections 3.1 to 3.5 describe the methods and equipment used to collect the in situ data. Subsection 3.6 describes the three-dimensional modeling approach used. Subsection 3.7 presents the methods used to analyze the diel SML dynamics. The preliminary results of the environmental conditions on days with and without MCS events, the model performance evaluation and the diurnal mixed layer patterns are given in section 4. The effects of MCS events on the heat balance and SML dynamics and the possible implications for water quality are discussed in section 5. A summary and final considerations are presented in section 6.

2. Study site

The Tucuruí Hydroelectric Reservoir (THR) is located in the Brazilian Amazon, Pará State, between 3°43'2"S, 49°59'15"W and 4°52'31"S, 49°9'13"W (Fig. 1). The THR is one of the largest hydroelectric reservoirs in the world, with a flooded area of 2,918 km² and a total volume of 50.3 billion m³ [Maciel, 2012]; the maximum depth is approximately 100 m when the reservoir is full. The reservoir is oriented north-south and is approximately 150 km long and 20 km wide. The THR residence time is approximately 51 days [Fearnside, 1999].

The climate in the THR region is classified as tropical with monsoons (Am) [Peel *et al.*, 2007]. The average monthly air temperature ranges from 24.5 °C (February) to 28 °C (October), with an annual average temperature of 26.5 °C. The rainfall, which exceeds 2000 mm yr⁻¹, is distributed irregularly with two well-defined seasons: wet (from October to April) and dry (from May to September). During the wet season (austral summer), the rainfall can exceed 400 mm month⁻¹, with a peak in January. This period corresponds to the occurrence of the SACZ and ITCZ over South America and the Amazon region, when it is possible to observe an increase in cloud clusters and MCS activity over these areas [Liebman *et al.*, 1999; Rickenbach *et al.*, 2011].

3. Methods

3.1. Reservoir bathymetry

A bathymetric grid with a 400 x 400 m spatial resolution was obtained from the spatial interpolation of depth samples collected with a GPSMap 520s Garmin® ecobathymeter (Olathe, Kansas, USA) during a single field expedition conducted between 3 and 16 July 2013. The field survey was conducted in this period because the reservoir level was near the maximum operational level (74 m above sea level), among other factors. During the data collection the ecobathymeter was preprogrammed to collect and store depth samples every 2 seconds using the geographical coordinates system and the World Geodetic System 1984 (WGS-84) as the datum; a total of

179,898 depth samples, with an accuracy of ± 0.1 m, were collected. Before spatially interpolating the values to generate the bathymetric grid, the depth samples were corrected to the maximum level of the reservoir operation. We used the ordinary kriging algorithm to generate the bathymetric grid and validated the results using the leave-one-out cross validation technique [Li and Heap, 2008]; the root-mean-square-error (RMSE) was less than 1 m.

3.2. Surface meteorology

The meteorological data were acquired hourly between 21 December 2012 and 21 March 2013 by an autonomous system called ‘Integrated System for Environmental Monitoring’ (SIMA, from the Portuguese spelling). SIMA [Stech *et al.*, 2006; Alcântara *et al.*, 2013] consists of a set of hardware and software designed for meteorological and limnological data acquisition and monitoring of natural and man-made aquatic systems. The primary characteristics of the meteorological sensors used are summarized in Table 1, and the SIMA position within the THR is shown in Figure 1. The meteorological data were recorded every hour, as a result from a mean of 30 samples collected by a burst sampling of 0.3 ms duration at a 10 μ s rate. In addition, the wind speed and direction were collected every 30 s, 10 times before and 10 times after the hourly recording; the mean value of these 21 samples was recorded. The data collected by SIMA were transmitted by satellite to the National Institute for Space Research (INPE, from the Portuguese spelling) facilities in Cuiabá (Mato Grosso State, Brazil) and Alcântara (Maranhão State, Brazil). Then, the data were electronically re-transmitted to the INPE unit in Natal (Rio Grande do Norte State, Brazil), where the data were processed to filter the gaps in the transmission signal. Finally, the data were electronically sent to the Remote Sensing Division (DSR) in São José dos Campos

(São Paulo State, Brazil). At DSR, the data were decoded, processed and stored in the SIMA database.

3.3. Water temperature time series

Time series of water temperature profiles' were collected hourly between 21 December 2012 and 21 March 2013 by two thermistor chains: one installed at the river-reservoir transition zone (the CH1 station) and one installed in the main body of the reservoir (the CH2 station) (see Fig. 1 for the locations). Each thermistor chain had 15 HOBO Onset® U22-001-Water Temp Pro v2 probes (Bourne, Massachusetts, USA). These thermistors operate between -40 °C and 50 °C with a factory-specified accuracy of ± 0.2 °C.. At CH1, thermistors were installed at 0.3, 1, 2, 3, 4, 5, 6, 7, 8, 10, 12, 14, 16, 18, and 20 meter depths. At CH2, thermistors were installed at 0.3, 1, 2, 4, 6, 8, 10, 12, 14, 16, 18, 20, 25, 30 and 35 meter depths. In addition to the two thermistor chains, a YSI® 6600 V2 sonde (Yellow Springs, Ohio, USA) was used to collect the hourly water surface temperature (i.e., at a 0.5 m depth) at the SIMA location. The YSI sonde temperature sensor operates between -5 °C and 60 °C with a factory-specified accuracy of ± 0.15 °C.

3.4. Identification of MCS

MCS activity over the THR was identified using an algorithm called ForTraCC (Forecast and Tracking the Evolution of Cloud Clusters), which was developed by *Vila et al.* [2008]. ForTraCC is a remote-sensing-based model that uses thermal infrared data (wavelength centered at 10.8 μm) collected by the Geostationary Operational Environmental Satellite (GOES) to identify and track MCS using their radiative and morphological properties. This algorithm also forecasts the

evolution of MCS physical properties based on cloud-top brightness temperatures for up to 120 minutes.

The ForTraCC algorithm has four main steps which are briefly described next. The first step of the algorithm is the detection of a MCS, which is based on the concept that deep convection penetrates into the upper troposphere (i.e., between 9 and 10 km above the land surface). ForTraCC uses a brightness temperature threshold of 235 K and a minimum storm size of 2400 km² (which equates to 150 pixels, considering the 4 km x 4 km resolution of a GOES image) to identify a MCS. The second step is the identification of morphological (e.g., size and location of the center of mass) and radiative (e.g., mean and minimum brightness temperatures) parameters of each MCS detected in the previous step. These parameters are described in detail by *Machado et al.* [1998] and *Vila and Machado* [2004]. The third step is MCS tracking, which is based on an overlap method [Mathon and Laurent, 2001]. This method assumes that the same cloud is present at two different times if there are common pixels in consecutive GOES images, while also considering the initial size and temperature thresholds. Successive GOES images are compared forward and backward in time to determine one of five situations: spontaneous generation, natural dissipation, continuity, splitting and merging. The final step is the MCS forecast, which is based on the estimates of the displacement of the MCS's center of mass and its life cycle phase. The MCS mass center displacement estimate considers three consecutive times or image acquisitions ($t-2\Delta t$, $t-\Delta t$ and t) and the life cycle phase (growth-decay) is evaluated through the normalized area expansion. A complete description of ForTraCC methodology and its validation are available in *Vila et al.* [2008].

In the present work, we accessed the ForTraCC database, which is available at <http://sigma.cptec.inpe.br/fortracc/>, for the period of 21 December 2012 to 21 March 2013 to

identify MCS activity over the Tucuruí Reservoir. MCS were identified by visual inspecting all of the images available in the ForTraCC database for the specific period. Figure 2 shows examples of MCS identified over the THR during the summer of 2013. The incident shortwave radiation data collected by the SIMA buoy was used to confirm the occurrence of these events.

3.5. Heat balance estimation

The hourly heat balance, ΔQ (W m^{-2}), of the THR at the SIMA station was estimated according to *Henderson-Sellers* [1986]:

$$\Delta Q = (1 - \alpha_{sw})Q_{SW} + (Q_{LWin} - Q_{LWout}) + Q_E + Q_H \quad (1)$$

where α_{sw} is the shortwave albedo (dimensionless), which is computed according to the day of the year and the reservoir latitude, Q_{SW} is the incident shortwave radiation (W m^{-2}), Q_{LWin} is the atmospheric incident longwave radiation (W m^{-2}), Q_{LWout} is the longwave radiation emitted by the water surface (W m^{-2}), Q_E is the latent heat flux (W m^{-2}) and Q_H is the sensible heat flux (W m^{-2}). Here, we used the convention that a heat flux is positive (negative) if it is entering (leaving) the reservoir.

The incident shortwave radiation was measured directly by SIMA, and the atmospheric incident longwave radiation surface was estimated following *Henderson-Sellers* [1986]:

$$Q_{LWin} = (1 - \alpha_{LW})\varepsilon_a\sigma T_a^4(1 + kC^2) \quad (2)$$

where α_{lw} is the longwave radiation albedo (= 0.03; *Henderson-Sellers* [1986]), ε_a is the air emissivity (dimensionless), σ is the Stefan-Boltzmann constant (= $5.67 \times 10^{-8} \text{ W m}^{-2} \text{ K}^{-4}$), T_a is the air temperature (K), k is a parameter that depend on the cloud characteristics (= 0.17; *Henderson-Sellers* [1986]) and C is the cloud cover fraction (dimensionless). The ε_a was calculated as a function of the air temperature and vapor pressure, following *Brutsaert* [1975]:

$$\varepsilon_a = 0.642 \left(\frac{e_a}{T_a} \right)^{1.7} \quad (3)$$

where e_a is the vapor pressure (hPa), based on the computation by *Verburg and Antenucci* [2010]. The mean daily value of the cloud cover was calculated using the incident shortwave radiation collected by SIMA and the empirical relationship presented by *Reed* [1977]; this relationship was developed using 40 months of data collected at three coastal sites (from the tropics to the extra tropics) and was verified against 125 days of data obtained in the eastern Pacific from the Tropics to the Gulf of Alaska. Overall, the relationship is considered appropriate from the tropics to high latitudes. The longwave radiation emitted by the water surface was estimated following *Henderson-Sellers* [1986]:

$$Q_{LWout} = \varepsilon_w \sigma T_w^4 \quad (4)$$

where ε_w is the water emissivity (= 0.97; *Henderson-Sellers* [1986]) and T_w is the water surface temperature measured by a YSI® sonde coupled with SIMA (K). The latent and sensible heat fluxes were estimated according to *Verburg and Antenucci* [2010]:

$$Q_E = \rho_a U_{10} L_V C_E (q_a - q_w) \quad (5)$$

$$Q_H = \rho_a U_{10} C_{pa} C_H (T_a - T_w) \quad (6)$$

where ρ_a is the air density (kg m^{-3}), U_{10} is wind speed 10 m above the water surface (m s^{-1}), L_V is latent heat of vaporization (J kg^{-1}), q_a is the specific humidity (kg kg^{-1}), q_w is the specific humidity at saturation (kg kg^{-1}), C_{pa} is the specific heat of air ($= 1003 \text{ J kg}^{-1} \text{ K}^{-1}$; *Fischer et al.* [1979]), and C_E and C_H are the transfer coefficients for latent and sensible heat transfer, respectively (dimensionless). ρ_a , L_V , q_a , and q_w are calculated using the methods described by *Verburg and Antenucci* [2010]. The wind data collected by SIMA at a height of 3 m was extrapolated to a 10 m height, U_{10} , using the following equation [*Schertzer et al.*, 2003]:

$$U_{10} = U_z \left(\frac{10}{z} \right)^{1/7} \quad (7)$$

where U_z is the wind speed (m s^{-1}) measured at a height of z meters (3 m in the SIMA platform). In this study we also considered $C_E = C_H$ ($C_{E,H}$). Because of the persistent unstable atmospheric conditions over tropical lakes [*Verburg and Antenucci*, 2010], we used the iterative procedure proposed by *Hicks* [1975] and the set of equations presented by *Verburg and Antenucci* [2010] to account for the stability of the ABL in the estimations of the latent and sensible heat fluxes. This iterative procedure was initialized using neutral stratification heat transfer coefficients [*Amorocho and Devries*, 1980]. Then, a set of similarity functions (ψ -functions) was used to correct the heat-

transfer coefficients for non-neutral conditions based on the stability parameter, ζ (dimensionless), defined as:

$$\zeta = \frac{z}{L_{MO}} \quad (8)$$

where z is the height of the meteorological sensors (m) and L_{MO} is the Monin-Obukhov length scale (m^{-1}). Following *Imberger and Patterson* [1989], a cutoff was imposed on the stability parameter ($\zeta_{\max} = |15|$), and the iterative procedure was repeated until the L_{MO} converged to within 0.001%.

3.6. Three-dimensional modeling of thermal structures

The Estuary and Lake Computational Model (ELCOM) [*Hodges et al.*, 2000; *Laval et al.*, 2003] was used to simulate the physical response of the Tucuruí Reservoir to MCS activity during the austral summer of 2012-2013. ELCOM simulates the vertical Reynolds stress terms (and the turbulent fluxes) using momentum and transport equations with a 3D mixed-layer approach derived from the mixing energy budgets developed for 1D lake modeling [*Imberger and Patterson*, 1989]. 1D mixed-layer models are typically Lagrangian re-grid the vertical domain to match the number of mixed regions in the water column, whereas the present 3D method uses an Eulerian fixed-grid framework because Lagrangian 3D methods typically produce highly skewed grid cells when horizontal gradients in the mixing occur. ELCOM applies a separate 1D mixed-layer model to each water column to provide the vertical turbulent transport, whereas the 3D transport of turbulent kinetic energy (TKE) provides the dynamic effect of 3D motions on the TKE available for vertical mixing.

3.6.1. Model setup

The numerical domain used in the simulation was discretized on a uniform horizontal grid containing 400 m x 400 m cells based on bathymetry data. To investigate the SML dynamics we used a non-uniform vertical grid resolution with thin layers in the upper part of the water column. The thickness of the vertical layers increased smoothly with the depth from 0.1 m (upper water column) to 5 m (bottom layer) resulting in a total of 74 layers. These grid configurations were chosen to optimize the model performance and to reduce the computational cost.

The mean water albedo for shortwave radiation was set to 0.03 [Slater, 1980], and the bottom drag coefficient was set to 1×10^{-3} [Wüest and Lorke, 2003]. The attenuation coefficient for photosynthetically active radiation (PAR), K_d , was set to 1.2 m^{-1} based on radiometric measurements with TriOS® Ramses radiometers (Rastede, Lower Saxony, Germany) during a field expedition that was conducted between 22 and 30 November 2012. K_d was calculated for the PAR range (400 to 700 nm) using 27 vertical profiles of downward irradiation collected at various reservoir zones, as described in Kirk [1994]. The K_d ranged from 0.49 m^{-1} to 4.03 m^{-1} , and the value used in this study is consistent with other studies conducted at Amazon basin rivers and lakes [Costa et al., 2013]. A value of $5.25 \text{ m}^2 \text{ s}^{-1}$ was chosen for the horizontal diffusivity of temperature and momentum, based on a previous study conducted in another Brazilian tropical reservoir [Pacheco et al., 2011].

We defined three sets of boundary cells to force the model: one inflow (Tocantins River), one outflow (the water intake at the bottom of the dam) and the free surface (meteorology). The model was forced using the hourly meteorological data acquired by SIMA, the mean daily cloud cover computed using the Reed [1976] empirical equation and the daily inflow and outflow provided by Eletrobrás-Eletronorte, the company that oversees the reservoir. The Tocantins River temperature was considered constant during the simulation period (29.1°C) and was obtained from the “Emissions of Greenhouse Gases in Hydroelectric Reservoirs” project database.

To account for unstable atmospheric conditions, the atmospheric stability sub-model was activated during the simulations; this procedure is appropriate in cases in which the meteorological sensors are located within the internal boundary layer over the lake surface and the data are collected at sub-daily intervals [Imberger and Patterson, 1989]. Considering the weak stratification ($\sim 0.1 \text{ }^{\circ}\text{C m}^{-1}$) observed in the main body of the THR (the CH2 station) we found that the reduced gravity g' has typical values on the order of $O(10^{-3} \text{ m s}^{-2})$. The reservoir depth on in the order of $O(10^0 \text{ m})$, and the Coriolis parameter has values on the order of $O(10^{-5} \text{ s}^{-1})$. These typical values provided internal wave velocities on the order of $O(10^{-2} \text{ m s}^{-1})$ and a Rossby radius of deformation on the order of $O(10^3 \text{ m})$ which is lower than the width of the reservoir $\sim O(10^4 \text{ m})$. Hence, the rotational effect should not be neglected, and the Coriolis sub-model was activated during the simulations.

Prior to the simulations, a sensitivity analysis was conducted to evaluate the influence of horizontal diffusivity on the modeled thermal structure. This analysis was performed using the perturbation parameter method [Schladow and Hamilton, 1996] by setting the horizontal diffusivity parameter values to 50% higher and lower than those found by Pacheco *et al.* [2011]. The results of this analysis showed that ELCOM has a low sensitivity to the horizontal diffusivity parameter, with differences less than 5% among the model results. The period chosen for this simulation was 21 December 2012 to 21 March 2013. However, to spin-up the circulation patterns and water temperature gradients, the simulation was initiated 10 days before the period of interest (i.e., on 11 December 2012). The time step was set to 90 seconds, which was sufficient to ensure the numerical stability of the model [Cassuli and Cattani, 1994]. The initial temperature profiles were obtained through linear interpolation of the thermistor chains at CH1 and CH2 stations. A flat, free surface was considered at the beginning of the simulation, and the water level was 58 m above sea level.

After the simulation, the ELCOM results were validated using the water temperature data acquired by the thermistor chain (CH1 station) and the water surface temperature collected by the YSI® sonde (SIMA station). The thermistor chain located at CH2 malfunctioned and only collected data only in the first three days following installation (from 21 December 2012 to 24 December 2012); these data were only used as initial conditions in the model.

3.7. Analysis of the diel surface mixed layer dynamics at the main body of the reservoir

To analyze the effects of MCS on SML dynamics at the main body of the THR we used the set of equations described in *Imberger* [1985] and the Wedderburn number W (dimensionless):

$$W = \frac{g' h^2}{u_{*w}^2 L} \quad (9)$$

where g' is the reduced gravitational acceleration due to the density jump across the base of the mixed layer and is computed using the density profiles simulated by ELCOM at the CH2 station (m s^{-2}), h is the depth of the SML (m), L is the basin length scale in the direction of wind (~ 10000 m) and u_{*w} is the water shear velocity (m s^{-1}). The depth of the SML, h (m), was defined as the first depth where the temperature difference was 0.02°C relative to the surface temperature (at 0.1 m) [*MacIntyre et al.*, 2002] and was computed using the temperature profile simulated by ELCOM at the CH2 station.

Prior to the W calculation the wind speed time series was averaged by considering the period of dominant internal waves (H1V1). This period was calculated based on *Martin and McCutcheon* [1999] and was found to be approximately 2 days for the THR; the wind speed time series was averaged every 12 hours ($1/4$ of the internal wave period). After the W calculation, we used the

classification scheme presented by *MacIntyre* [2008] to describe the response of the SML to environmental forces: (1) $W > 10$, the wind only mixes the upper layers of a lake, and thermocline tilting, which is required to induce internal waves, does not occur; (2) $2 < W < 10$, partial tilting of the thermocline occurs and induces shear across the interface, which may induce Kelvin-Helmholtz billows and turbulence; (3) $W \sim 1$, the thermocline upwells; and (4) $W \ll 1$, full vertical mixing can occur.

The velocity scale associated with the generation of mechanical turbulent kinetic energy (TKE) was evaluated using the water shear velocity, u_{*w} (m s^{-1}), defined as [*Imberger*, 1985]:

$$u_{*w} = \left(\frac{\tau}{\rho_w} \right)^{1/2} \quad (10)$$

where τ is the surface wind stress (Pa) and ρ_w is the surface water density simulated by ELCOM at the CH2 station (kg m^{-3}). However, the velocity scale associated with the convective overturn was evaluated using the penetrative convection velocity, w_* (m s^{-1}), defined as [*Imberger*, 1985]:

$$w_* = (Bh)^{1/3} \quad (11)$$

B is the buoyancy flux ($\text{m}^2 \text{s}^{-3}$) given by:

$$B = \frac{g\alpha H^*}{C_{pw}\rho_w} \quad (12)$$

where g is the gravitational acceleration ($= 9.8 \text{ m s}^{-2}$), α is the water thermal expansion coefficient between 20°C and 30°C , as shown by *MacIntyre et al.* [2002], C_{pw} is the specific heat of water ($= 4186 \text{ J kg}^{-1} \text{ K}^{-1}$) and H^* is the effective surface heat flux (W m^{-2}), defined as:

$$H^* = S + q(0) + q(h) - \frac{2}{h} \int_0^h q(z) dz \quad (13)$$

where S is the surface heat flux computed using the surface meteorology data ($= Q_{LWin} - Q_{LWout} + Q_E + Q_H$, W m^{-2}), $q(0)$ is the shortwave radiation at the surface ($= (1 - \alpha_{sw})Q_{sw}$, W m^{-2}), and $q(h)$ is the shortwave radiation at the bottom of the SML (W m^{-2}). The radiation penetration into the water column was computed using Beer's Law:

$$q(z) = q(0)e^{-K_d z} \quad (14)$$

where K_d is the attenuation coefficient for the shortwave radiation in the PAR region ($= 1.2 \text{ m}^{-1}$) and z is the depth of the water column (m).

In our study we used the mechanical energy flux, F_q ($\text{m}^3 \text{ s}^{-3}$), in order to investigate what is the main source of TKE (i.e., wind stirring or surface cooling) controlling the deepening of the SML during a MCS event. The F_q was obtained using the following equation [*Imberger, 1985*]:

$$F_q = 0.5(w_*^3 + C_N^3 u_*^3) \quad (15)$$

where C_N is a constant ($= 1.33$, *Imberger, [1985]*).

4. Results

4.1. Environmental conditions during the summer and MCS events

A notable diel pattern was observed in all meteorological variables monitored during the summer of 2012-2013. The hourly mean air temperature (Fig. 3a) ranged from 25.3 °C to 29.0 °C, with a daily mean air temperature of 26.9 °C for the period. The highest air temperature was observed at approximately 17:00 h, and the lowest temperature was observed at approximately 7:00 h (local time; -3 GMT). The water surface temperature (Fig. 3b) fluctuated within than 0.5 °C throughout the day and typically ranged from 29.4 °C to 29.7 °C, with a daily mean water surface temperature of 29.6 °C for the entire summer.

The wind speed (Fig. 3c) ranged from 1.8 m s⁻¹ to 3.2 m s⁻¹, with a daily mean value of 2.5 m s⁻¹. The diel variation exhibited a pattern that was opposite to that of the air temperature, with the peak wind speed occurring at night (3:00 h) and the minimum occurring in the afternoon (between 14:00 h and 15:00 h). During the summer, the wind usually flowed from southeast to northwest during the morning and from south to north in the afternoon.

The atmospheric pressure (Fig. 3d) fluctuated between 996 hPa and 1000 hPa, on average, throughout the day. The highest atmospheric pressure value was observed at 10:00 h, and the lowest was observed at 17:00 h. On the synoptic scale, no sign of frontal passages, which are associated with a significant pressure rise (ahead of the front) and drop (behind the front), were observed in the dataset. This finding was expected considering the low latitude of the THR and the time of the year. Consistent with the pattern of the diel variations in the air temperature, the maximum relative humidity was generally observed at approximately 6:00 h, while the minimum relative humidity was observed at approximately 16:00 h (Fig 3e). The average values for the maximum and minimum relative humidity were 84% and 68%, respectively.

Because of to cloud formation, the peak incident shortwave radiation (Fig. 3f) was frequently shifted from its normal time at noon to approximately 13:00 h. The average daily maximum shortwave radiation value was 643 Wm^{-2} . However, in cloudless conditions, the peak incident shortwave radiation can be higher than 1100 Wm^{-2} . On average, at this time of the year in the study region, the sunrise and sunset occur approximately 06:00 and 18:00, respectively; thus, approximately 12 hours of the incident shortwave radiation are available.

The estimated cloud cover over the THR was strongly related to MCS activity during the summer. Higher values of cloud cover spanned the beginning of the observation period to the beginning of February. The MCS activity decreased at the end of the summer; thus, the cloud cover also significantly decreased from the beginning of February to mid-March.

Over the THR, MCS activity occurred on 22 days, which is 24% of the study period. These events occurred every three- or four-days, and they were observed mostly between 00:00 h and 14:00 h. The mean duration of MCS activity over the Tucuruí region was approximately 10 h. January had the strong MCS activity (11 days; 50% of the total days with MCS events). In contrast, March had the weakest MCS activity (4 days; 18% of the total). Table 2 shows a summary of the near-surface meteorology at the THR on the days with and without MCS activity during the study period. With the exception of the wind speed ($p\text{-value} = 0.38$), all other meteorological variables were significantly different ($p\text{-value} < 0.01$) on the days with MCS activity.

4.2. Reservoir heat balance

The latent heat (Fig. 4a) is the main surface heat flux component. On average, latent heat accounted for approximately 60% of the surface energy exchange with the atmosphere. As expected, the latent heat flux component was always negative, with the reservoir constantly losing energy to the atmosphere via evaporation. The latent heat flux ranged from -3 W m^{-2} to -553 W m^{-2} .

², with a mean value of -111 W m^{-2} . On the days with MCS activity, the latent heat flux generally exceeded -300 W m^{-2} . However, higher fluxes ($Q_E < -300 \text{ W m}^{-2}$) were also observed on days without MCS activity due to high wind events (e.g., 22 December 2012).

The net longwave radiation was negative throughout the study period (Fig. 4b), showing that the longwave radiation emitted by the reservoir surface was generally higher than the atmospheric incident longwave radiation. This component of the surface heat balance ranged from -108 W m^{-2} to -1 W m^{-2} , with a mean value of -58 W m^{-2} throughout the summer. The net longwave radiation flux was the second most important component of the surface heat balance; it accounted for approximately 32% of the surface energy exchange with the atmosphere. The time series of the net longwave flux clearly shows the distinct period at the beginning of February when the MCS activity strongly declined. The net longwave flux was the flux component most strongly correlated with MCS activity.

The sensible heat flux (Fig. 4c) ranged from -120 W m^{-2} to 10 W m^{-2} , with a mean value of -16 W m^{-2} . A few positive values that corresponded to heat gain by the reservoir were observed during the observation period, generally between 12:00 h and 17:00 h when the air was warmer than the water. The sensible heat flux was the least important component of the surface heat flux during the summer of 2012-2013; it accounted for approximately 8% of the total energy released by the reservoir to the atmosphere.

During the study period the ABL was unstable approximately 99% of the time (Fig. 4d). This behavior is similar to other tropical lakes and reservoirs [MacIntyre *et al.*, 2002; Verburg and Antenucci, 2010]. The heat flux transfer coefficient (Fig. 4e) ranged from 1.5×10^{-3} to 4.0×10^{-3} , with a mean value of 2.1×10^{-3} . These values are higher than those observed by Verburg and Antenucci [2010] for Lake Tanganyika ($\sim 1.84 \times 10^{-3}$) and are similar to those reported by MacIntyre *et al.* [2002] for Lake Victoria; both lakes are in the tropics.

The heat balance (Fig. 4f) ranged from -772 W m^{-2} to 1033 W m^{-2} during the day, with a mean value of -8 W m^{-2} . Therefore, the water column cooled approximately $0.6 \text{ }^{\circ}\text{C}$ during the study period.

4.3. Thermal structure simulation

4.3.1. Model validation

The error analysis for the simulated temperature (Fig. 5) showed that for the two sampled validation points (the CH1 and SIMA stations; see Fig. 1 for the locations), ELCOM tended to overestimate (bias < 0) the water temperature in the upper part of the water column (Fig. 5a, b, c) and underestimate (bias > 0) the water temperature in the deeper layers (Fig. 5d, e, f, g, h, i, j). The mean absolute error (MAE) ranged from $0.07 \text{ }^{\circ}\text{C}$ (2.8% of the range) to $0.29 \text{ }^{\circ}\text{C}$ (11.74% of the range) and the RMSE was lower than $0.4 \text{ }^{\circ}\text{C}$ for all of the validation points. The model performed better in the transition zone than in the main body of the reservoir, with a RMSE range from $0.18 \text{ }^{\circ}\text{C}$ (6% of the range) to $0.09 \text{ }^{\circ}\text{C}$ (3.5% of the range) and a mean value of $0.12 \text{ }^{\circ}\text{C}$ (4.6% of the range) at the CH1 station; the validation point at the main body of the reservoir (the SIMA station) had a RMSE of $0.4 \text{ }^{\circ}\text{C}$ (~16% of the range). The error values found in this study were similar to those reported in other modeling studies [*Schladow and Hamilton, 1997; Missaghi and Hondzo, 2010; Lee et al., 2013*]. Therefore ELCOM performed well when predicting the water column temperature in the THR.

4.3.2. Spatio-temporal dynamics of the thermal structure

As shown previously, during most of the summer, the THR released energy to the atmosphere. Hence, the water column cooled down, particularly during January and February, when the MCS activity was more frequent. During the study period, a persistent thermal gradient

(~1.5 °C) was observed between the river-reservoir transition zone and the main body of the reservoir (Figs. 6 and 7). This thermal gradient was enhanced by the Tocantins River inflow, which is typically 2 °C colder than the reservoir temperature during the summer.

In the main body of the reservoir and in the region near the dam, the vertical thermal structure showed a similar pattern in which the signal of the seasonal thermocline and the water column were completely mixed during most of the day (Fig. 6). In these two reservoirs zones, the temperature difference between the surface and bottom was typically less than 0.5 °C during the night and morning (Fig. 6a, c), then increased during the day (Fig. 6b, d). In the river-reservoir transition zone, the thermal structure presented a distinct behavior when compared with the main body of the reservoir and with the region near the dam. In this zone, the mixing process was mainly governed by the Tocantins River inflow, and the water column was completely mixed all day.

On the days without MCS events, we observed alternating behavior in the upper part of the water column (Fig. 6a, b), associated with diurnal stratification and the formation of the SML during the day. In this case, the temperature difference between the surface and bottom was over 2.5 °C in the afternoon. However, on the days with MCS activity (Fig. 6c, d) the diurnal stratification was less intense at THR when compared with days without MCS activity; in some cases, the development of the SML was not observed.

At the reservoir surface (Fig. 7), the water temperature tended to be spatially heterogeneous all day, and the river-reservoir transition zone was approximately 1.5 °C cooler than the main body of the reservoir in the morning. This spatial heterogeneity increased during the day and the difference between the water temperature in the transition zone and main body of the reservoir reached up to 3 °C on days without MCS activity over the THR (Fig. 7b). However, on the days in which a MCS occurred over the THR (Fig. 7c, d), the spatial heterogeneity in the surface temperature was lower when compared with days without MCS activity. In this case, the difference

between the water surface temperature in the transition zone and in the main body of the reservoir was approximately 1 °C cooler in the morning and 1.5 °C cooler in the afternoon (Fig. 7c, d).

4.4. Diel behavior of the surface mixed layer at the main body of the THR

During the summer, the W values ranged from 0.383 to 0.001 (Fig. 8a), with a mean value of 0.038, which is indicative of intense mixing between the epilimnion and the hypolimnion and of upwelling events at the upwind side of the basin. Lower values of W were generally observed during the night and early morning, when the heat loss by the reservoir surface and the wind force was higher. The W values tended to increase during the day, indicating detrainment in the mixed layer, an increase in thermal stratification and a decrease in vertical mixing.

The depth of the SML (Fig. 8b) ranged from 0.2 m to 5 m during the summer, with a mean depth of 1.1 m. The SML dynamics typically showed three distinct periods during the day, as described by *Imberger* [1985]. First, a heating phase (stage 1) generally occurred between 10:00 h and 16:00 h. During this stage, the input energy provided by the sun stabilized the SML and confined it to the top few centimeters of the water column (~0.3 m). As a result, the water warmed approximately 1.5 °C (from 28.9 to 30.4 °C, see Fig. 3b). The isotherms show the formation of a strong, shallow diurnal thermocline during the heating phase, with the surface temperature reaching a maximum at approximately 16:00 h.

The increase in the wind speed in the late afternoon (see Fig. 3c) approximately 16:00 h, marks the start of the sea breeze deepening period (stage 2). During this stage, the wind speed was higher than 3 m s⁻¹ destroying the strong thermal gradient formed during stage 1. In response to the wind forcing, the isotherms at the base of the SML tilted and the SML deepened. The maximum tilt of the diel thermocline was observed at approximately 19:00 h, which is approximately three hours after the wind speeds began to increase. The sea breeze deepening period ended in the middle

of the night, between 01:00 h and 03:00 h, when the wind speed began to decrease. At the end of this stage, the SML thermocline reached a new equilibrium position around a depth of 1.4 m.

As shown in Fig. 3a and c, during the late night and early morning the air temperature and wind speed decreased over the THR, reaching values of approximately 1.7 m s^{-1} and 25°C , respectively. The calm conditions, along with the drop in the air temperature ($\sim 5^\circ\text{C}$), initiates the convective cooling period (stage 3). In this case, the deepening of the SML was dominated by natural convective processes. The SML reached its maximum depth, typically 2.5 m, at the end of convective cooling period, between 08:00 h and 09:00 h (Fig. 8b).

Figures 8c and d shows the mean diel variation in the water shear velocity scale, u_{*w} , and the penetrative convection velocity scale, w_* , associated with the generation of TKE in the summer. The values of u_{*w} ranged from 0 cm s^{-1} to 1.5 cm s^{-1} , with mean a value of 0.4 cm s^{-1} . The values of w_* ranged from 0.1 cm s^{-1} to 1 cm s^{-1} , with a mean value of 0.5 cm s^{-1} . These two velocity scales showed similar behavior during the day in which higher values occurred during the night and early morning and lower values occurred during the afternoon. The w_* values are higher than u_{*w} all day, indicating that during a typical summer day, most TKE available for mixing the water column is generated by convection of the water column. The convective (h/w_*) timescale of the vertical mixing within the SML ranged between 87 s and 2445 s, with a mean value of 286 s; the shear (h/u_{*w}) timescales ranged from 0 s to 18090 s, with a mean value of 493 s. The two timescales exhibited distinct behaviors during the days in which the convective timescale exhibited a single peak (at approximately 09:00 h), while the shear timescale exhibited two peaks (at 09:00 h and 20:00 h).

The energy flux into the SML, Fq , ranged from $0 \text{ m}^3 \text{ s}^{-3}$ to $4.4 \times 10^{-6} \text{ m}^3 \text{ s}^{-3}$ with a mean value of $1.8 \times 10^{-7} \text{ m}^3 \text{ s}^{-3}$ (Fig. 8e). Higher values were observed in the late evening and overnight due to high wind speeds and convection induced by the surface cooling (high buoyancy flux). However,

lower values were observed during the afternoon due to the low wind speeds and low buoyancy flux. The surface cooling was the main process contributing to the flux of TKE into the SML; it accounted for 56% of the energy input during the day, on average. The wind shear also contributed to the energy flux and accounted for 44% of the total energy input.

5. Discussion

5.1. Impacts of MCS activity on the heat balance components

It is well known that the exchange of heat between an open water surface and the overlying atmosphere is influenced by environmental factors such as the wind speed, air temperature and relative humidity [Imberger and Patterson, 1989; MacIntyre *et al.*, 2002; Verburg and Antenucci, 2010]. Therefore, subtle changes in the near-surface meteorology, usually in the cloud cover and incident shortwave radiation, caused by the MCS activity over the THR (see Table 2) impacted the heat fluxes. To investigate the impacts of MCS on heat fluxes on a diel time scale, we computed the hourly mean heat fluxes for days with and without MCS activity over the THR (Fig. 9).

The latent heat flux typically ranged from -147 W m^{-2} to -84 W m^{-2} on the days with MCS events (Fig. 9a). The hourly mean latent heat flux on these days was approximately -113 W m^{-2} . In contrast, on the days with MCS activity, the latent heat flux ranged from -144 W m^{-2} to -74 W m^{-2} , with a mean value of -108 W m^{-2} . During the days with MCS activity, the mean latent heat flux was enhanced by approximately 4.6% compared with days without MCS events.

The net longwave energy flux (Fig. 9b) behaved in the opposite manner to the latent heat flux, i.e., the longwave energy loss decreased on days with MCS activity. On the days with MCS events, the net longwave flux ranged, on average, from -53 W m^{-2} to -27 W m^{-2} , with an hourly mean value of -38 W m^{-2} . Conversely, on the days without MCS activity, the net longwave flux ranged, on average, from -75 W m^{-2} to -53 W m^{-2} , with a mean value of -64 W m^{-2} . The mean net

longwave flux decreased (in absolute values) by approximately 40.6% on the days with MCS events. This reduction is the result of an increase in the atmospheric incident longwave radiation due to the growth of cloud cover and a reduction in longwave radiation emitted by the colder reservoir water.

The sensible heat flux behaved similarly to the latent heat flux, i.e., increased on the days with MCS activity over the reservoir (Fig. 9c). The sensible heat flux ranged, on average, from -7 W m^{-2} to -29 W m^{-2} , with a mean value of -18 W m^{-2} , on the days with MCS activity. On the days without MCS events, the sensible heat flux ranged from -1 W m^{-2} to -28 W m^{-2} , with a mean value of -14 W m^{-2} . The MCS events enhanced the sensible heat loss by approximately 28.6%.

The reservoir diel heat balance (Fig. 9d) was strongly affected by MCS. On the days with MCS activity over the reservoir, the heat balance was typically negative, i.e., the reservoir acted as an energy source for the atmosphere. The heat balance ranged, on average, from -233 W m^{-2} to 333 W m^{-2} , with a mean value of -41 W m^{-2} , on the days with MCS events. On the days without MCS events, the heat balance ranged, on average, from -260 W m^{-2} to 608 W m^{-2} , with a mean value of 31 W m^{-2} . Note that the MCS events changed not only the magnitude of the heat balance but also the cooling period extent, which was an average of 1 hour longer than on the days without MCS events. This reduction in the heating period was also observed by *Curtarelli et al.* [2014] in a tropical reservoir located in central Brazil during cold front.

Table 3 summarizes the daily mean values of the heat balance components for the days with and without MCS activity over the THR. As also observed by *MacIntyre* [2012] for tropical lakes in Africa, the changes observed in the heat balance components during MCS activity over the THR were mainly driven by the increase in the cloud cover, which strongly reduced the incident shortwave radiation over the water. The increase in the wind speed and the decrease in the air temperature played a secondary role in such cases.

The impacts of MCS events on the heat balance at THR are similar to the impacts of wintertime cold fronts on tropical reservoirs in southeastern and central Brazil [Curtarelli *et al.*, 2014]. Both meteorological phenomena are able to enhance the heat loss by more than 100% when compared with the heat flux on the days without the events. However, the impacts on each heat balance component differ. The net longwave flux is the heat loss component most impacted under MCS conditions (increase of 40.6%), while the sensible heat flux is most impacted (increase of 77%) under cold front conditions. .

5.2. Impacts of MCS on surface mixed layer dynamics

In response to the changes in the near-surface meteorology and in the reservoir heat balance, which becomes negative (reservoir heat loss), the SML dynamics exhibited a distinct behavior on the days with MCS activity compared with the days without MCS activity (Fig. 10). Typically, on the days without MCS (Fig. 10a), the SML depth ranged from 0.6 m to 2.4 m, with a mean depth of 1.3 m. However, on the days with MCS activity (Fig. 10b), the SML depth ranged from 1 m to 2.7 m, with a mean depth of 1.6 m (24% increase). This finding is related to the effective heat flux, which is generally 28% higher (in absolute values) on the days with MCS activity; a daily mean value of -77 W m^{-2} occurs under MCS condition.

The MCS activity over the THR changed not only the depth of the SML but also the temporal dynamics during the day. All three SML stages identified in the section 4.4 (i.e., heating phase, sea breeze deepening and convective cooling) changed under the MCS conditions. First, the heating phase shortened on a MCS day. The phase began approximately 1.5 h later and ended approximately 1.5 h before if compared with a day without a MCS event. The sea breeze deepening stage was also delayed; it generally began (ended) 1.5 h to 2 h later (earlier) when compared with the days with MCS events. The maximum depth of the SML during the convective cooling period,

which was delayed by approximately 1 h on the days with MCS events, generally occurred at 10:30 h.

The penetrative entrainment velocity scale was typically higher (~30% higher) than the water shear velocity scale all day in both situations, with or without MCS activity (Fig. 10c, d); therefore the SML deepening was dominated by surface cooling processes instead of wind forcing at the surface. The occurrence of MCS over the THR did not change the water shear velocity scale, which ranged from 0.2 cm s^{-1} to 0.4 cm s^{-1} with a mean value of 0.3 cm s^{-1} in both situations (days with or without MCS activity). However, the penetrative entrainment velocity scale was affected by the occurrence of MCS; it increased approximately 25%, from 0.4 cm s^{-1} to 0.5 cm s^{-1} (mean daily value).

On days with MCS activity, penetrative entrainment due to mixing mechanisms was responsible for approximately 60% of the energy input to the SML ($\sim 1 \times 10^{-7} \text{ m}^3 \text{ s}^3$). The timescale of mixing due to surface cooling, between 1 and 10 minutes, tended to be faster than that due to the wind. The deepening SML on the MCS days contributed to the increase in the duration of the mixing induced by the wind, which was nearly 25 minutes on MCS days.

5.3. Possible impacts of MCS activity on water quality and greenhouse gas emissions

As shown in the previous sections, when a MCS passes over the THR, significant changes are observed in the local energy balance (Fig. 9) and SML dynamics (Fig. 10). Hence, changes are expected in the water quality and greenhouse gas (GHG) emissions of the THR during MCS events. For Arctic and midlatitude lakes, *Eugster et al.*, [2003] showed that there are significant differences in greenhouse gases emissions between non-convective and convective conditions over the lakes. The carbon dioxide (CO_2) fluxes can be approximately 5 times higher during periods with penetrative convection when compared with stably stratified periods. The observed increases in the

CO₂ fluxes during convective conditions are also related to the entrainment of metalimnetic water which can increase the gas concentration in the SML.

For tropical lakes and reservoirs, *Tundisi et al.* [2010] proposed a model for phytoplankton succession based on the instability in the water column and the occurrence of meteorological disturbances over southeastern Brazilian reservoirs. The authors showed that changes in sunlight and increases in nutrients related to the intense vertical mixing during meteorological disturbances create a pre algae bloom condition in the upper part of a water column.

The results of the present study, when considering the results of *Eugster et al.* [2003] and *Tundisi et al.* [2010], indicate that MCS can be important events that affect the water quality and GHG emissions in the THR and in Amazonian reservoirs and lakes. This effect is expected to be maximized during the austral summer when MCS are more frequent compared with the austral winter. The increase in convection, the deepening of the SML, and the full water column mixing induced by MCS occurrence may be the key physical processes that drive the water quality and the GHG emissions of Amazonian lakes and reservoirs. Therefore, we suggest that further studies on water quality and GHG emissions conducted at Amazonian water bodies should account for the effects of these meteorological phenomena.

6. Summary and Conclusions

In this study we evaluated the effects of MCS on the heat balance and SML dynamics of a large hydroelectric reservoir located in the Brazilian Amazon during the austral summer. We used in situ data and remote sensing products to identify the occurrence of MCS activity over THR during the summer of 2013, and we used a 3D hydrodynamic model to simulate the SML response to these events. The main conclusions are as follow:

MCS are important events that control the heat balance and SML dynamics of the THR reservoir during the austral summer. These events are frequent over the THR during the summer;

they occur on more than 20% of the days in the season. MCS are often associated with an increase in the cloud cover fraction and a decrease in the incident shortwave radiation and air temperature over the THR. In response to these meteorological changes, the diel heat balance changes, with greater heat loss from the reservoir to the atmosphere and a cooler water surface. The incident shortwave radiation, sensible heat and net longwave fluxes are the most strongly affected components of the heat balance during the MCS activity.

The SML dynamics exhibited two distinct behaviors during the summer, depending on the presence/absence of MCS events. MCS over the THR contribute to deep SML, i.e., up to 3 m depth. Surface cooling is the main physical process driving the SML dynamics in the THR, and penetrative entrainment is responsible for approximately 60% of the energy input to the SML during a MCS event.

The effects of MCS events on the energy balance and SML dynamics of Amazonian reservoirs are similar to those described by *Curtarelli et al.*, [2014] for tropical hydroelectric reservoirs located in southeastern Brazil that are subject to cold front incursions during the austral winter. However, the cold front passages over the southeastern reservoirs have a stronger impact on the energy balance and SML dynamics than the MCS events over the Amazonian reservoirs.

The results in this study indicate that the MCS are one of the main meteorological phenomena that drive the physical processes in the Amazonian hydroelectric reservoirs and lakes during the summer. Hence, the occurrence of MCS events over these aquatic systems may have several implications for the local water quality (e.g., creating pre-algae bloom conditions) and GHG emissions. Therefore, further studies are needed to understand and quantify the effects of MCS events on ecological and biogeochemical processes, such as, the primary production and GHG emissions.

Acknowledgements

We thank J. A. D. Leão and F. S. Pacheco for their assistance collecting the bathymetric data and installing the SIMA platform and thermistor chains during the field campaigns. The field campaigns were supported by the Northern Brazil Electric Power Company (ELETRONORTE, grant 4500075234) and the Brazilian Electricity Regulatory Agency (ANEEL, grant 8000003629). The SIMA platform and thermistor chains were funded by the Brazilian Electricity Regulatory Agency (ANEEL, grant 8000003629). The authors are grateful to the Centre for Water Research (CWR), University of Western Australia (UWA), for providing the ELCOM model for this study

and to the National Institute of Science and Technology for Climate Change (INCT for Climate Change) for funding the ELCOM model license. The first author is grateful to the Brazilian Council of Technological and Scientific Development (CNPq) for the doctorate-level scholarship (under grant 161233/2013-9). I. O. wishes to thank the Brazilian Federal Agency for Support and Evaluation of Graduate Education (CAPES) for the master-level scholarship. C. A. S. A. wishes to thank the CNPq (grant 302538/2014-3) for the PCI scholarship. Finally, the authors wish to thank the Remote Sensing Division (DSR) and the Hydrosphere Research Group of National Institute for Space Research (INPE) for providing the infrastructure for this study. The meteorological and limnological data collected for this study are available at <https://www.dsr.inpe.br/hidrosfera/sima/en/> and <http://www.dsr.inpe.br/hidrosfera/balanco/>. The reservoir operational data were obtained from the daily on line bulletin of ELETRONORTE, which is available at <http://www.eln.gov.br/opencms/export/sites/electronorte/pilares/geracao/estados/tucurui/boletim/bvn.pdf>.

References

- Alcântara, E., M. Curtarelli, I. Ogashawara, J. Stech, and A. Souza (2013), A system for environmental monitoring of hydroelectric reservoirs in Brazil, *Ambiente & Água* 8(1), 6-17, doi: 10.4136/ambi-agua.1088.
- Amorocho, J., and J. J. Devries (1980), A new evaluation of wind stress coefficient over water surfaces, *J. Geophys. Res.*, 85, C1, 433-442, doi: 10.1029/JC085iC01p00433.

Atoui, A., H. Hafez, and K. Slim (2012), Occurrence of toxic cyanobacterial blooms for the first time in Lake Karaoun, Lebanon, *Water Environ. J.*, 49(1), 42-49, doi: 10.1111/j.1747-6593.2012.00324.x.

Brutsaert, W (1975), On a derivable formula for long-wave radiation from clear skies, *Water Resour. Res.*, 11(5), 742-744, doi: 10.1029/WR011i005p00742.

Casulli, V., and E. Cattani (1994), Stability, accuracy and efficiency of a semi-implicit method for three-dimensional shallow water flow, *Comput. Math. Applic.*, 27(4), 99-112, doi: [http://dx.doi.org/10.1016/0898-1221\(94\)90059-0](http://dx.doi.org/10.1016/0898-1221(94)90059-0).

Casulli, V., and R. T. Cheng (1992), Semi-implicit finite difference methods for three-dimensional shallow water flow, *Int. J. Numer. Meth. Fluids.*, 15(6), 629-648, doi:10.1002/flid.1650150602.

Costa, M. P. F., E. M. L. M. Novo, and K. H. Telmer (2013), Spatial and temporal variability of light attenuation in large rivers of the Amazon, *Hydrobiol.*, 702(1), 171-190, doi: 10.1007/s10750-012-1319-2.

Curtarelli, M. P., E. Alcântara, C. D. Rennó, A. T. Assireu, M. –P. Bonnet, and J. L. Stech (2013), Modelling the surface circulation and thermal structure of a tropical reservoir using three-dimensional hydrodynamic lake model and remote-sensing data, *Water Environ. J.*, in press, doi: 10.1111/wej.12066.

Curtarelli, M. P., E. H. Alcântara, C. D. Rennó, and J. L. Stech, (2014) Physical changes within a large tropical hydroelectric reservoir induced by wintertime cold front activity, *Hydrol. Earth Syst. Sci.*, 18, 3079-3093, doi: 10.5194/hess-18-3079-2014.

Eugster, W., G. Kling, T. Jonas, J. P. McFadden, A. Wüest, S. MacIntyre, and F. S. III. Chapin (2003), CO₂ exchange between air and water in an Arctic Alaskan and midlatitude Swiss lake: importance of convective mixing, *J. Geophys. Res.*, 108, 4362, doi:10.1029/2002JD002653.

Fearnside, P. M. (1999), Social impacts of Brazil's Tucuruí dam, *Environ. Manage.*, 24(4), 485-495, doi: 10.1007/s002679900248.

Fischer, H. B., E. G. List, R. C. Y. Koh, J. Imberger, and N. H. Brooks (1979), *Mixing in inland and coastal waters*, Academic Press, New York.

Henderson-Sellers, B. (1986), Calculating the surface energy balance for lake and reservoir modeling: a review, *Rev. Geophys.*, 24(3), 625-649, doi: 10.1029/RG024i003p00625.

Hicks, B. B. (1975), A procedure for the formulation of bulk transfer coefficients over water, *Boundary-Layer Meteorol.*, 8(3-4), 515-524, doi: 10.1007/BF02153568.

Hodges, B. R., J. Imberger, A. Saggio, and K. B. Winters (2000), Modeling basin-scale internal waves in a stratified lake, *Limnol. Oceanogr.*, 45(7), 1603-1620, doi:10.4319/lo.2000.45.7.1603.

Houze, R. A. (2004), Mesoscale Convective Systems, *Rev. Geophys.*, 42(4), RG4003, doi: 10.1029/2004RG000150.

Imberger, J. (1985), The diurnal mixed layer, *Limnol. Oceanogr.*, 30, 737-770.

Imberger, J., and J. C. Patterson (1989), Physical limnology, *Adv. Appl. Mech.*, 27, 303-475, doi: [http://dx.doi.org/10.1016/S0065-2156\(08\)70199-6](http://dx.doi.org/10.1016/S0065-2156(08)70199-6).

Kirk, J. T. O. (1994), *Light and photosynthesis in aquatic ecosystems*, Cambridge University Press, Cambridge.

Komatsu, E., T. Fukushima, and H. Shiraishi (2006), Modeling of P-dynamics and algal growth in a stratified reservoir-mechanisms of P-cycle in water and interaction between overlying water and sediment, *Ecol. Model.*, 197(3-4), 331-349, doi: <http://dx.doi.org/10.1016/j.ecolmodel.2006.03.023>.

Laurent, H., L. A. T. Machado, C. A. Morales, and L. Durieux (2002), Characteristics of the Amazonian mesoscale convective systems observed from satellite and radar during the WETAMC/LBA experiment, *J. Geophys. Res.*, 107, D20, doi: 10.1029/2001JD000337.

Laval, B., J. Imberger, B. R. Hodges, and R. Stocker (2003), Modeling circulation in lakes: spatial and temporal variations, *Limnol. Oceanogr.*, 48(3), 983-994, doi: 10.4319/lo.2003.48.3.0983.

Lee, H., S. Chung, I. Ryu, and J. Choi (2013), Three-dimensional modeling of thermal stratification of a deep and dendritic reservoir using ELCOM model, *J. Hydro-environ. Res.*, 7(2), 124-133, doi: <http://dx.doi.org/10.1016/j.jher.2012.10.002>.

Leonard, B. P. (1991), The ULTIMATE conservative difference scheme applied to unsteady one-dimensional advection, *Comput. Method. Appl. Mech. Eng.*, 88(1), 17-74, doi: [http://dx.doi.org/10.1016/0045-7825\(91\)90232-U](http://dx.doi.org/10.1016/0045-7825(91)90232-U).

Li, J., and A. D. Heap (2008), A review of spatial interpolation methods for environmental scientists, Geoscience Australia, Canberra.

Liebmann, B., G. N. Kiladis, J. A. Marengo, T. Ambrizzi, and J. D. Glick (1999), Submonthly convective variability over South America and the South Atlantic Convergence Zone, *J. Clim.*, 12(7), 1877-1891, doi: [http://dx.doi.org/10.1175/15200442\(1999\)012%3C1877:SCVOSA%3E2.0.CO;2](http://dx.doi.org/10.1175/15200442(1999)012%3C1877:SCVOSA%3E2.0.CO;2).

Machado, L. A. T. (2000), The Amazon energy budget using the ABLE-2B and Flu Amazon data, *J. Atmos. Sci.*, 57(18), 3131-3144, doi: [http://dx.doi.org/10.1175/15200469\(2000\)057%3C3131:TAEBUT%3E2.0.CO;2](http://dx.doi.org/10.1175/15200469(2000)057%3C3131:TAEBUT%3E2.0.CO;2).

Machado, L. A. T., W. B. Rossow, R. L. Guedes, and A. W. Walker (1998), Life cycle variations of mesoscale convective systems over the Americas, *Mon. Wea. Rev.*, 126(6), 1630-1654, doi: [http://dx.doi.org/10.1175/1520-0493\(1998\)126%3C1630:LCVOMC%3E2.0.CO;2](http://dx.doi.org/10.1175/1520-0493(1998)126%3C1630:LCVOMC%3E2.0.CO;2).

Maciel, E. R. (2010), O lago, Ética, Imperatriz.

MacIntyre, S. (2008), Describing fluxes within lakes using temperature arrays and surface meteorology, *Verh. Internat. Verein. Limnol.*, 30, 339-344.

MacIntyre, S., R. Romero, and G. W. Kling (2002), Spatial-temporal variability in surface layer deepening and lateral advection in an embayment of Lake Victoria, East Africa, *Limnol. Oceanogr.*, 47(3), 656-671, doi: <http://dx.doi.org/10.4319/lo.2002.47.3.0656>.

Martin, J., and S. McCutcheon (1999), Hydrodynamics and transport for water quality modeling. Lewis Publishers, Boca Raton.

Mathon, V., and H. Laurent (2001), Life cycle of the Sahelian mesoscale convective cloud systems, *Quart. J. Roy. Meteor. Soc.*, 127(572), 377-406, doi: 10.1002/qj.49712757208.

Missaghi, S., and M. Hondzo (2010), Evaluation and application of a three-dimensional water quality model in a shallow lake with complex morphometry, *Ecol. Model.*, 221(11), 1512-1525, doi: <http://dx.doi.org/10.1016/j.ecolmodel.2010.02.006>.

Nogués-Paegle, J., and K. C. Mo (1997), Alternating wet and dry conditions over South America during summer, *Mon. Wea. Rev.*, 125(2), 279-291, doi: [http://dx.doi.org/10.1175/1520-0493\(1997\)125%3C0279:AWADCO%3E2.0.CO;2](http://dx.doi.org/10.1175/1520-0493(1997)125%3C0279:AWADCO%3E2.0.CO;2).

Pacheco, F. S., A. T. Assireu, and F. Roland (2011), Derivadores rastreados por satélites aplicados a ambientes aquáticos continentais: caso do reservatório de Manso, In *Novas Tecnologias para o monitoramento e estudo de reservatórios hidrelétricos e grandes lagos*, edited by E. H. Alcântara et al., pp. 193-218, Parêntese, São José dos Campos.

Peel, M. C., B. L. Finlayson, and T. A. McMahon (2007), Updated world map of the Köppen-Geiger climate classification, *Hydrol. Earth Syst. Sci.*, 11, 1633–1644, doi: 10.5194/hess-11-1633-2007

Reed, R. K. (1977), On estimating insolation over ocean, *J. Phys. Oceanogr.*, 7, 482-485, doi: [http://dx.doi.org/10.1175/1520-0485\(1977\)007<0482:OEIOTO>2.0.CO;2](http://dx.doi.org/10.1175/1520-0485(1977)007<0482:OEIOTO>2.0.CO;2)

Reynolds, C. S. (1992), Dynamics, selection and composition of phytoplankton in relation to vertical structure in lakes, *Arch. Hydrobiol.*, 35, 13-31.

Rickenbach, T. M., R. Nieto-Ferreira, R. P. Barnhill, and S. W. Nesbitt (2011), Regional contrast of mesoscale convective system structure prior to and during monsoon onset across South America, *J. Climate.*, 24(14), 2753-2763, doi: <http://dx.doi.org/10.1175/2011JCLI3975.1>.

Rudorff, C. M., J. Melack, S. MacIntyre, C. C. F. Barbosa, and E. M. L. M. Novo (2011), Seasonal and spatial variability of CO₂ emission from a large floodplain lake in the lower Amazon, *J. Geophys. Res.*, 116, G4, doi: 10.1029/2011JG001699.

Schertzer, W. M., W. R. Rouse, P. D. Blanken, and A. E. Walker (2003), Over-lake meteorology and estimated bulk heat exchange of Great Slave Lake in 1998 and 1999, *J. Hydrometeorol.*, 4(4), 649–659, doi:10.1175/1525-7541(2003)004<0649:OMAEBH>2.0.CO;2.

Schladow, S. G., and D. P. Hamilton (1997), Prediction of water quality in lakes and reservoirs: Part II - Model calibration, sensitivity analysis and application, *Ecol. Model.*, 96(1-3), 111-123, doi: [http://dx.doi.org/10.1016/S0304-3800\(96\)00063-4](http://dx.doi.org/10.1016/S0304-3800(96)00063-4).

Sippel, S. J., S. K. Hamilton, and J. M. Melack (1992), Inundation area and morphometry of lakes on the Amazon River floodplain, Brazil, *Archiv Hydrobiol.* 123, 385–400.

Slater, P. N. (1980), Remote sensing: optics and optical systems, Addison-Wesley, Reading.

Spiegel, R. H., and J. Imberger (1987), Mixing processes relevant to phytoplankton dynamics in lakes, *N. Z. J. Mar. Freshwat. Res.*, 21(3), 361-377, doi: 10.1080/00288330.1987.9516233.

Stech, J. L., I. B. T. Lima, E. M. L. M. Novo, C. M. Silva, A. T. Assireu, J. A. Lorenzzetti, J. C. Carvalho, C. C. F. Barbosa, and R. R. Rosa (2006), Telemetric monitoring system for meteorological and limnological data acquisition, *Verh. Internat. Verein. Limnol.*, 29, 1747-1750.

Tadesse, A., and E. N. Anagnostou (2010), African convective system characteristics determined through tracking analysis, *Atmos. Res.*, 98(2-4), 468-477, doi: <http://dx.doi.org/10.1016/j.atmosres.2010.08.012>.

Tundisi, J. L., T. Matsumura-Tundisi, K. C. Pereira, A. P. Luzia, M. D. Passerini, W. A. C Chiba, M. A. Morais, and N. Y. Sebastien (2010), Cold fronts and reservoir limnology: an integrated approach towards the ecological dynamics of freshwater ecosystems, *J. Baz. Biol.*, 70, 815–824, doi: <http://dx.doi.org/10.1590/S1519-69842010000400012>.

Verburg, P., and J. P. Antenucci (2010), Persistent unstable atmospheric boundary layer enhances sensible and latent heat loss in a tropical great lake: Lake Tanganyika, *J. Geophys. Res.*, 115, D11, doi: 10.1029/2009JD012839.

Vidal, J., E. Moreno-Ostos, C. Escot, R. Quesada, and F. Rueda (2010), The effects of diel changes in circulation and mixing on the longitudinal distribution of phytoplankton in a canyon-shaped Mediterranean reservoir, *Freshwat. Biol.*, 55(9), 1945-1957, doi: 10.1111/j.1365-2427.2010.02428.x.

Vila, D., and L. A. T. Machado (2004), Shape and radiative properties of convective systems observed from infrared satellite images, *Int. J. Remote Sens.*, 25(21), 4441-4456, doi: 10.1080/01431160410001726085.

Vila, D., L. A. T. Machado, H. Laurent, and I. Velasco (2008), Forecast and Tracking the Evolution of Cloud Clusters (ForTraCC) using Satellite Infrared Imagery: methodology and validation, *Wea. Forecasting*, 23(2), 233-245, doi: <http://dx.doi.org/10.1175/2007WAF2006121.1>.

Wüest, A., and A. Lorke (2003), Small-scale hydrodynamics, *Annu. Rev. Fluid Mech.*, 35, 373-412, doi: 10.1146/annurev.fluid.35.101101.161220.

Table 1. Technical specification of the SIMA sensors.

Sensor	Manufacturer/Model	Range	Accuracy	Height
Thermo hygrometer	Rotronic MP 101A	-40 to 60 °C	± 0.3 °C	3 m
		0 to 100%	± 1 %	
Anemometer	RM Young 05106	0 to 100 m s ⁻¹	± 0.3 m s ⁻¹	3 m
		0 to 360°	$\pm 3^\circ$	
Pyranometer	Novalynx 840-8102	0 to 1500 W m ⁻²	< 1 W m ⁻²	3 m

Barometric pressure	Vaisala PTB 110	800 to 1060 hPa	± 0.3 hPa at 20°C	3 m
---------------------	-----------------	-----------------	--------------------------	-----

Table 2. Statistical summary of surface meteorology in the days with and without MCS activity over THR (from 21 December 2012 to 21 March 2013).

Variables	MCS days			
	Mean	Max.	Min.	S.D.
Wind speed (m s^{-1})	2.5	7.8	0.0	1.6
Wind direction ($^{\circ}$)	164	357	0	130
Air temperature ($^{\circ}\text{C}$)	26.6	31.1	23.2	1.5
Relative humidity (%)	80	90	62	5
Atm. pressure (hPa)	999	1003	994	2

Shortwave radiation (W m^{-2})	132	797	0	201
Cloud cover (%)	65	100	0	37
Water surface temperature ($^{\circ}\text{C}$)	29	31	28	1
Variables	no MCS days			
	Mean	Max.	Min.	S.D.
Wind speed (m s^{-1})	2.5	11.4	0.0	1.6
Wind direction ($^{\circ}$)	151	357	0	131
Air temperature ($^{\circ}\text{C}$)	27.1	31.7	22.8	1.9
Relative humidity (%)	77	90	56	7
Atm. pressure (hPa)	999	1003	994	1.7
Shortwave radiation (W m^{-2})	215	1152	0	311
Cloud cover (%)	20	100	0	30
Water surface temperature ($^{\circ}\text{C}$)	30	31	28	1

Table 3. Mean values of heat balance components computed for the days with and without MCS activity over Tucuruí reservoir.

Heat balance component	Daily mean values		Difference	
	MCS days	Non MCS days	W m^{-2}	%
Shortwave incident (W m^{-2})	128	217	-89	41
Latent heat flux (W m^{-2})	-113	-108	5	4.6

Longwave incident (W m^{-2})	425	399	26	6.5
Longwave emitted (W m^{-2})	-463	-463	0	0.0
Net longwave flux (W m^{-2})	-38	-64	-26	40.6
Sensible heat flux (W m^{-2})	-18	-14	4	28.6
Heat balance (W m^{-2})	-41	31	72	232.3

Figure captions

Figure 1. Study area. (a) Location on South America and (b) Tucuruí Hydroelectric Reservoir boundaries and bathymetry.

Figure 2. Examples of MCS identified using the ForTraCC algorithm. (a) 18 January 2013 11:15 h, (b) 28 January 2013 07:00 h, (c) 22 February 18:30 h and (d) 16 March 2013 19:45 h. The

red circle indicates the THR location. The color code indicates the stage of the life cycle of the MCS.

Figure 3. Mean diel variation of near-surface meteorology computed for the whole period, days with and without MCS activity over THR: (a) air temperature, (b) water surface temperature (c) wind speed at 10 m, (d) atmospheric pressure, (e) relative humidity, (f) incident shortwave radiation.

Figure 4. Time series of (a) latent heat flux, (b) net longwave radiation, (c) sensible heat flux and (d) stability parameter, (e) latent and sensible heat transfer coefficient and (f) total heat balance, computed for the whole analyzed period.

Figure 5. Three-dimensional model validation: (a) SIMA station, and CH1 station at a depth of (b) 1 m, (c) 3 m, (d) 4 m, (e) 5 m, (f) 6 m, (g) 7 m, (h) 8 m, (i) 10 m and (j) 11 m.

Figure 6. Spatio-temporal dynamics of the water column temperature simulated by ELCOM along the latitudinal transect AA' (see Figure 1) during a day without MCS activity (a) 4 February 2013 at 09:00 h and (b) 4 February 2013 at 16:00 h, and a day with MCS activity (c) 7 February 2013 at 09:00 h and (d) 7 February 2013 at 16:00 h.

Figure 7. Spatio-temporal dynamics of the simulated water surface at 0.1 m depth during a day without MCS activity (a) 4 February 2013 at 09:00 h and (b) 4 February 2013 at 16:00 h, and a day with MCS activity (c) 7 February 2013 at 09:00 h and (d) 7 February 2013 at 16:00 h.

Figure 8. Time series of (a) 12 hour averaged Wedderburn number, (b) SML depth, (c) penetrative entrainment and wind shear velocity scales and (d) energy flux into SML, computed for the whole analyzed period.

Figure 9. Diel variation of (a) latent heat flux, (b) longwave net radiation, (c) sensible heat flux and (d) total heat balance, computed for the whole season, days with and without MCS activity over THR.

Figure 10. SML diel dynamics simulated by ELCOM at main body of THR (CH2 station): isotherms displacements during the days (a) without MCS and (b) with MCS over THR; penetrative entrainment and wind shear velocity scales during the days (c) without MCS and (d) with MCS over THR.

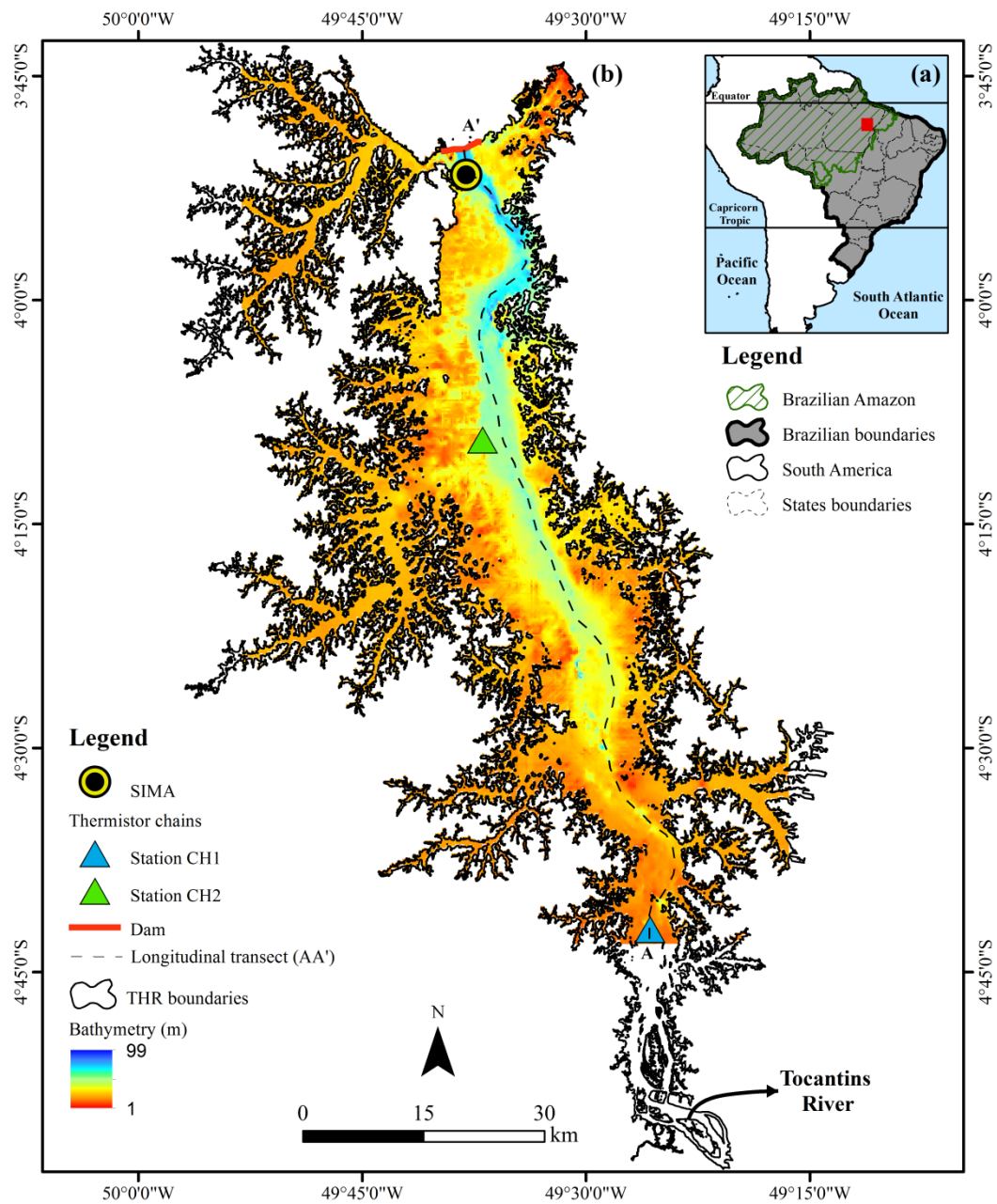


Figure 1.

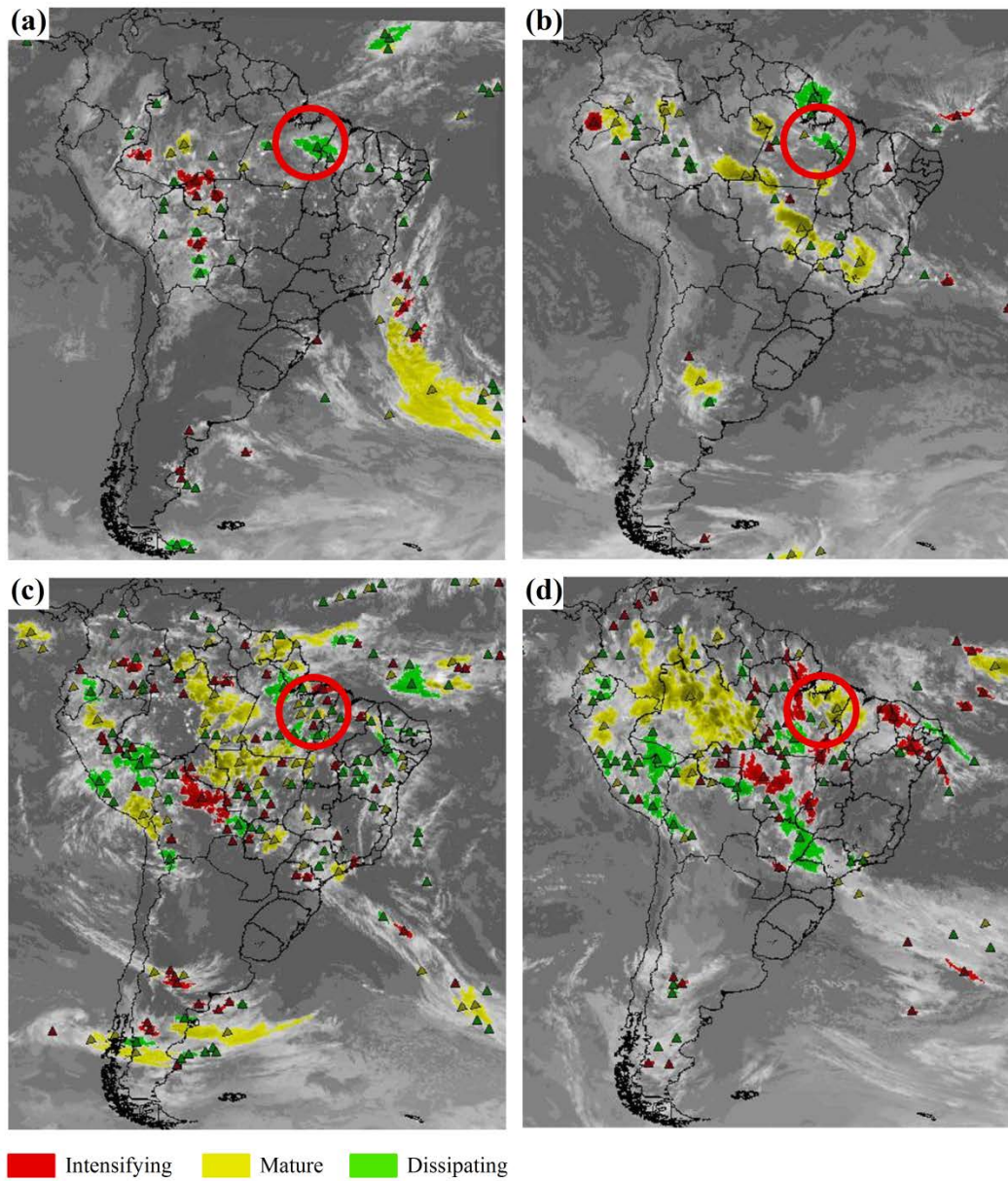


Figure 2.

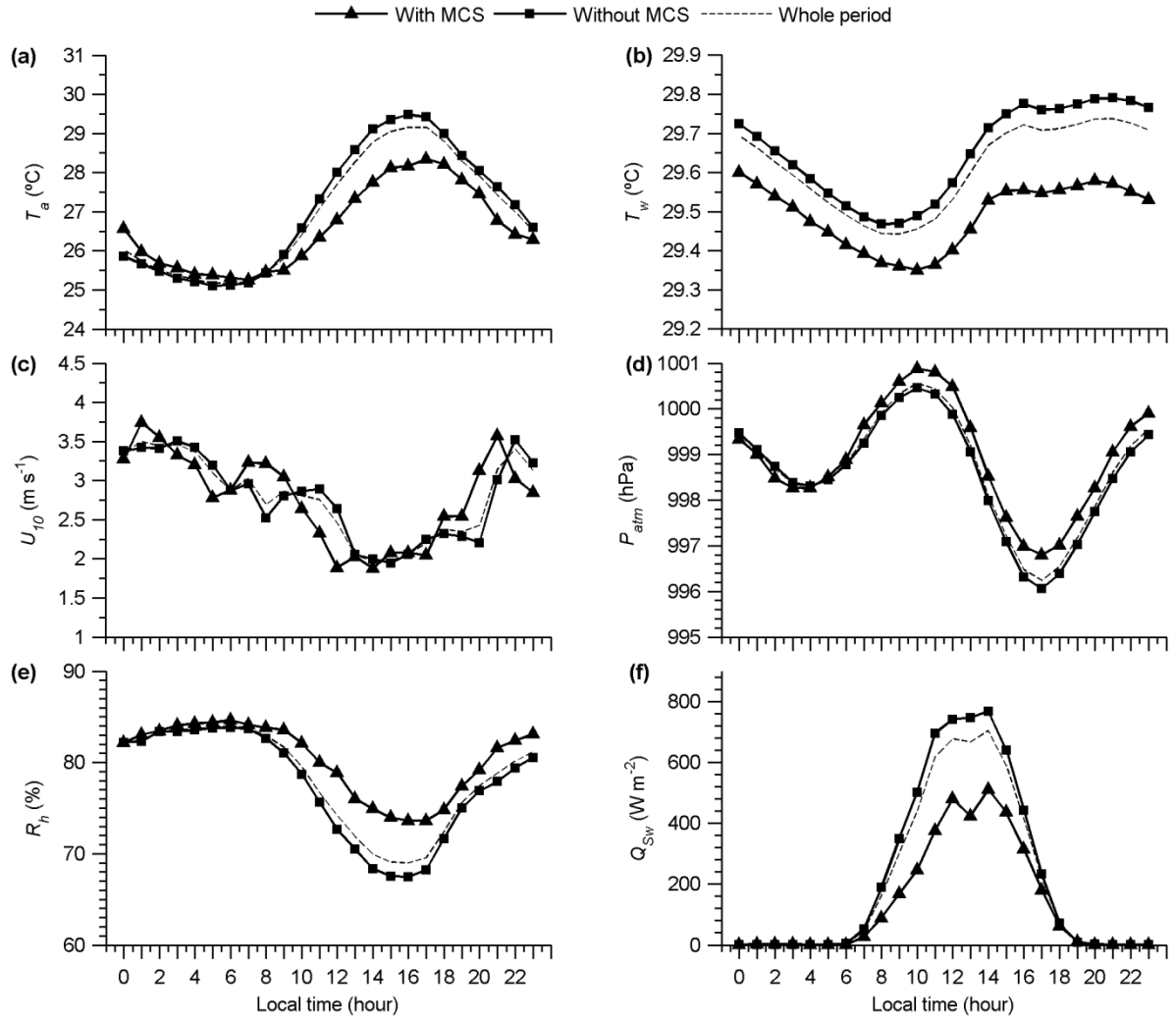


Figure 3.

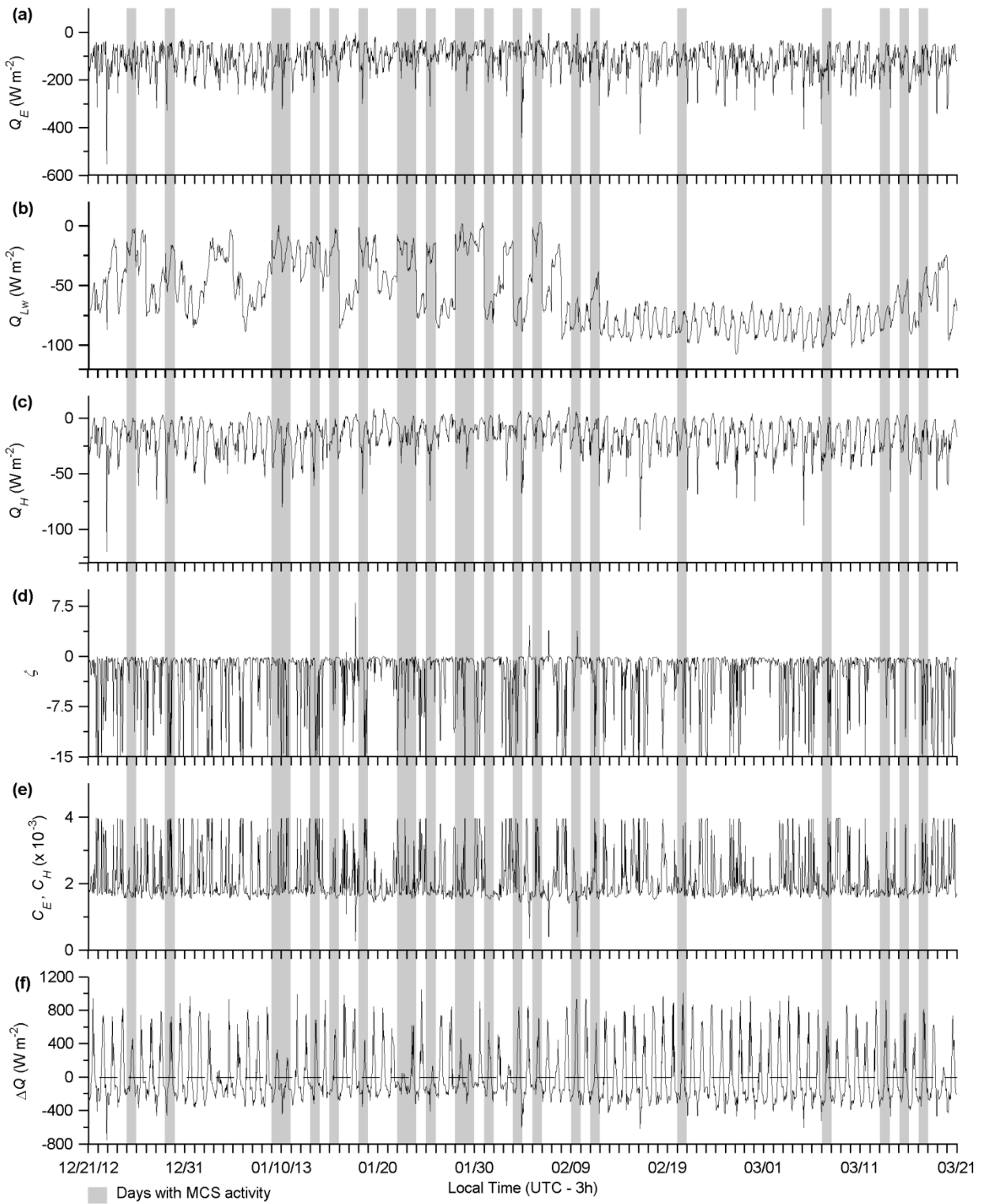


Figure 4.

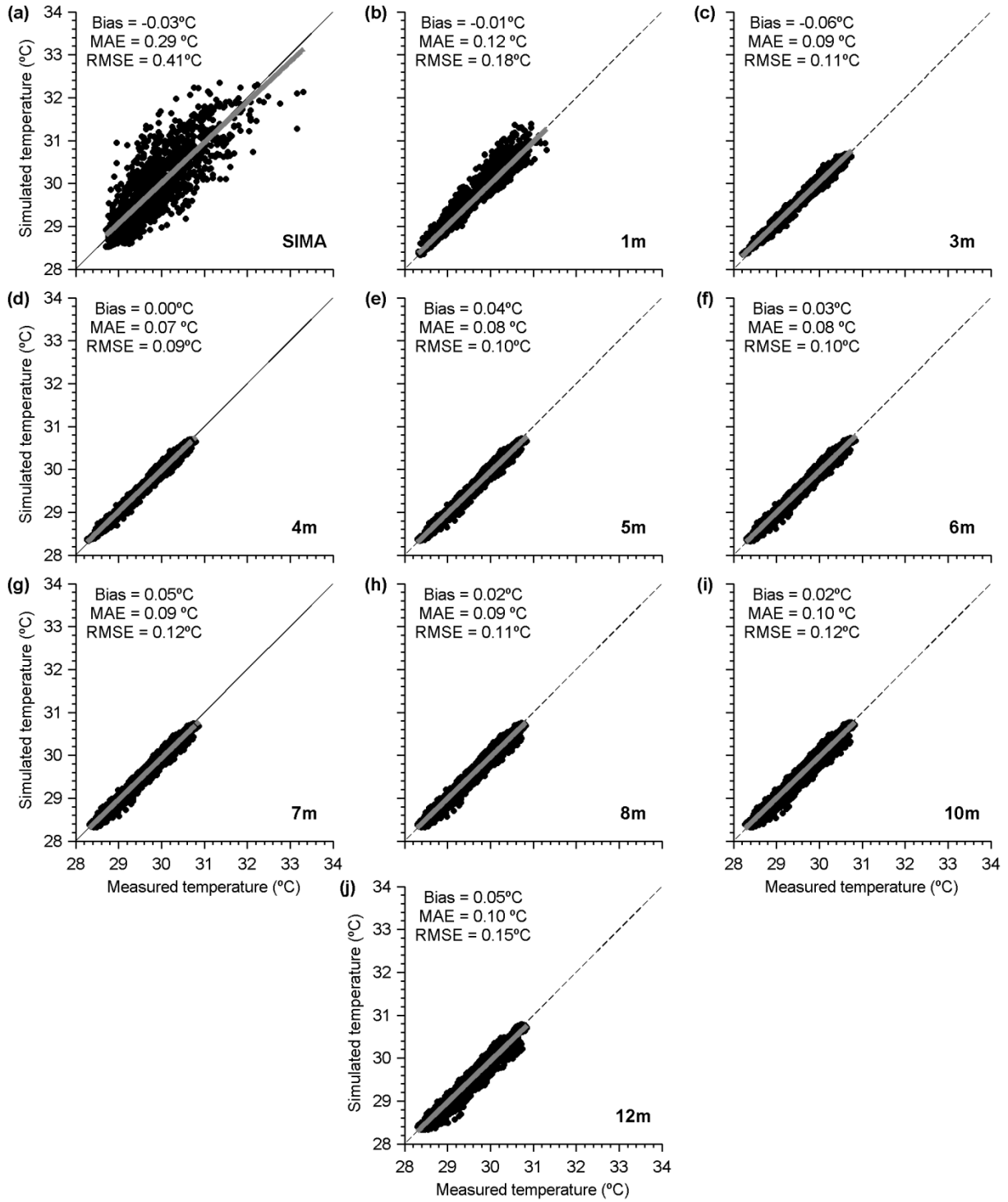


Figure 5.

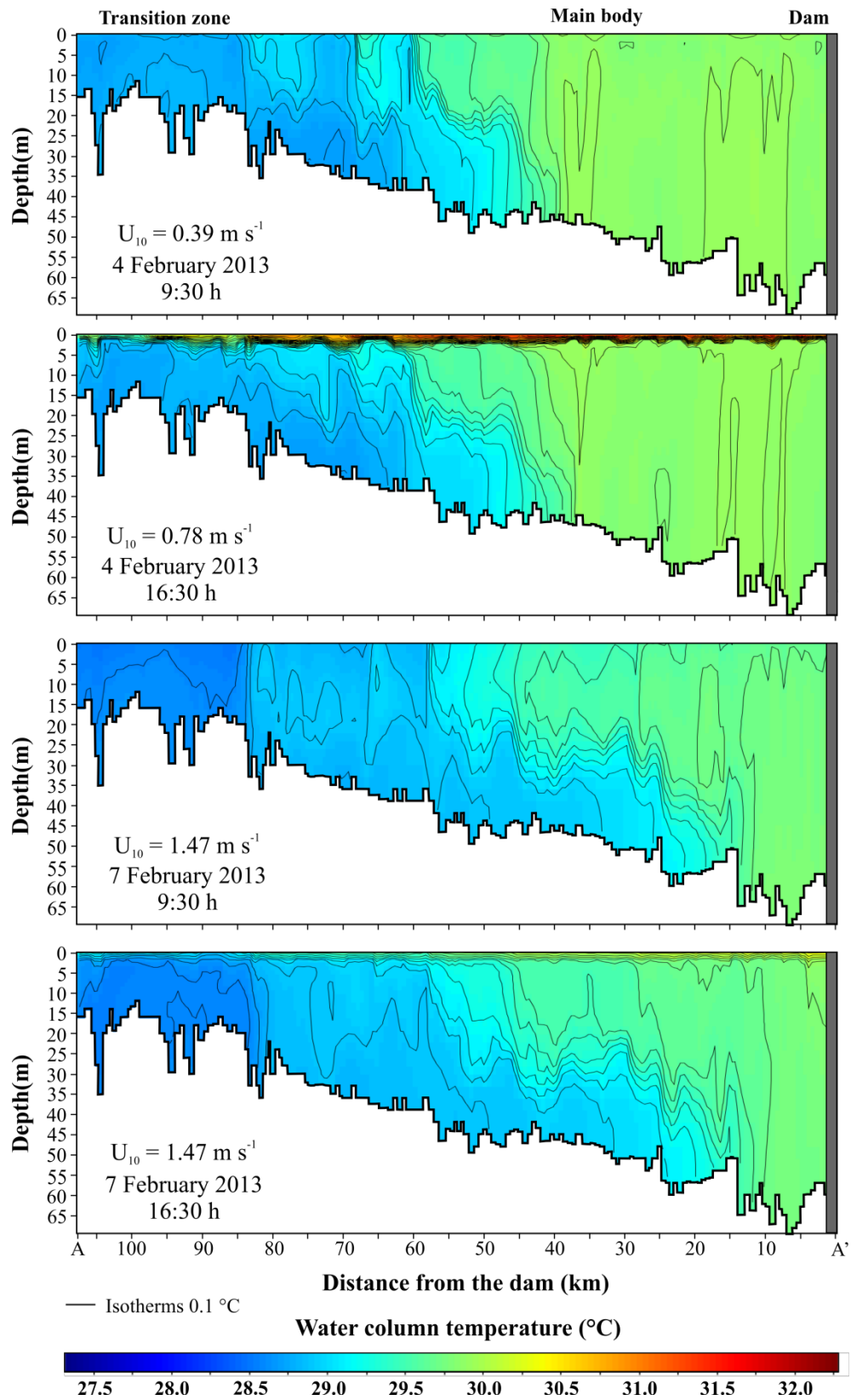


Figure 6.

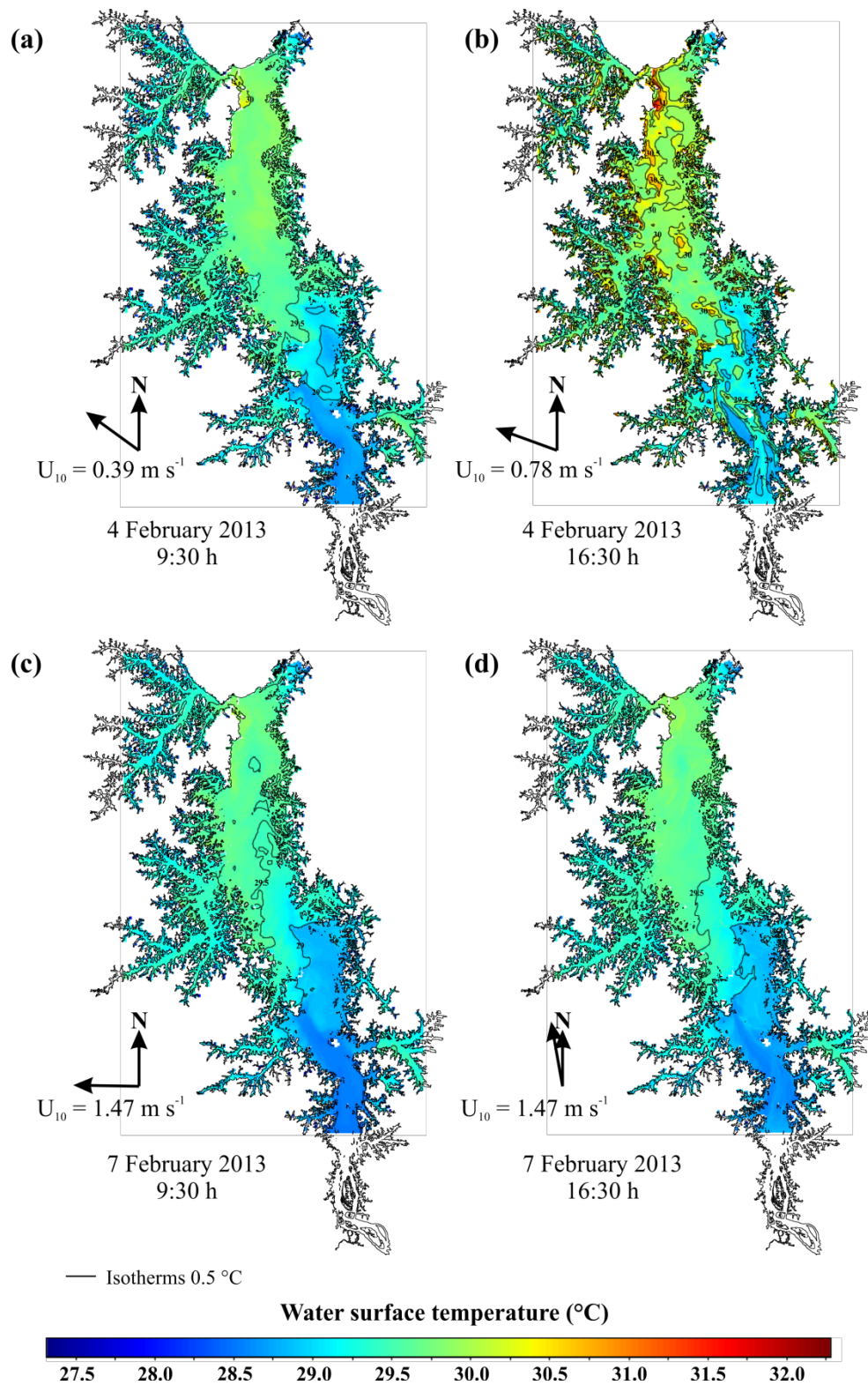


Figure 7.

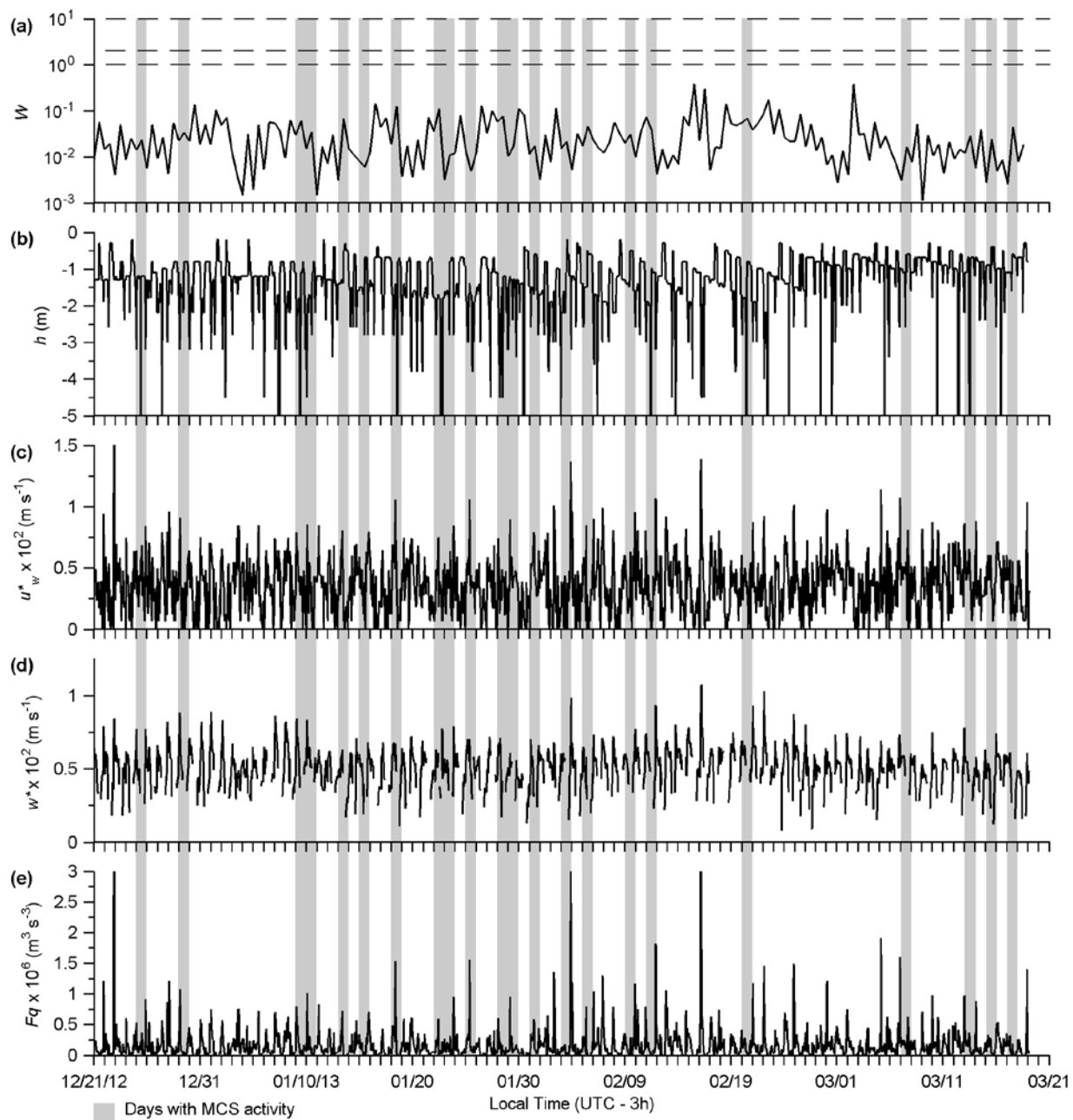


Figure 8.

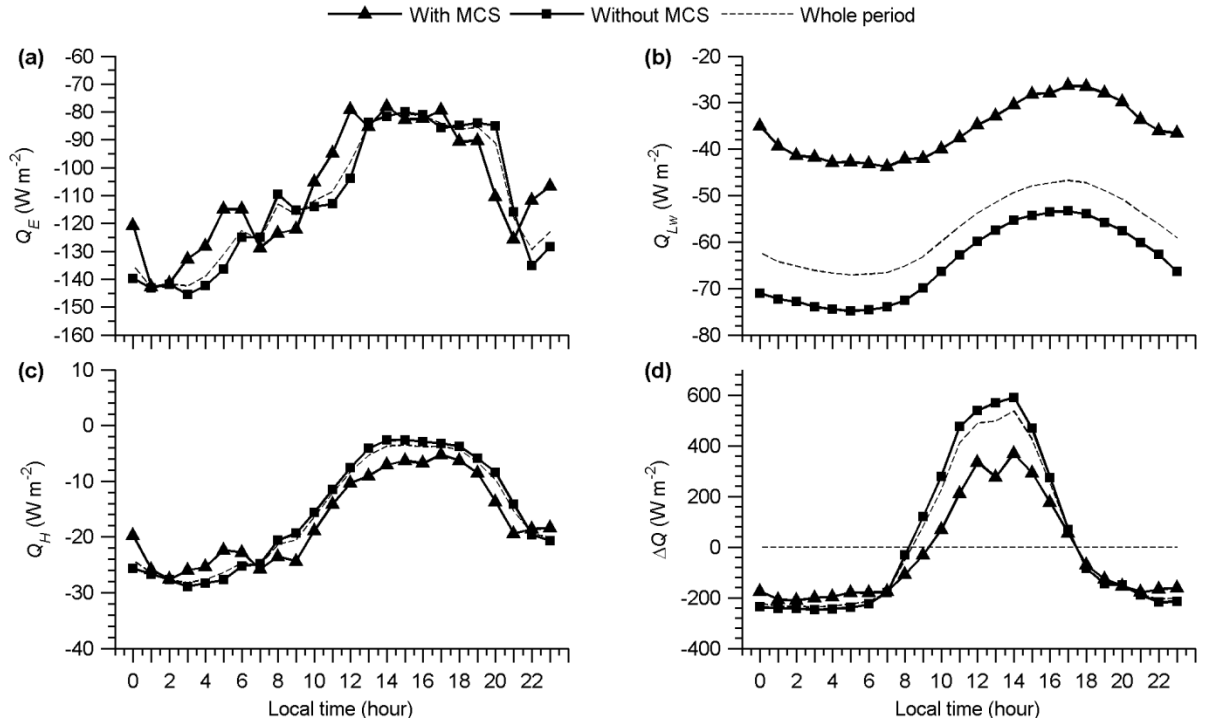


Figure 9.

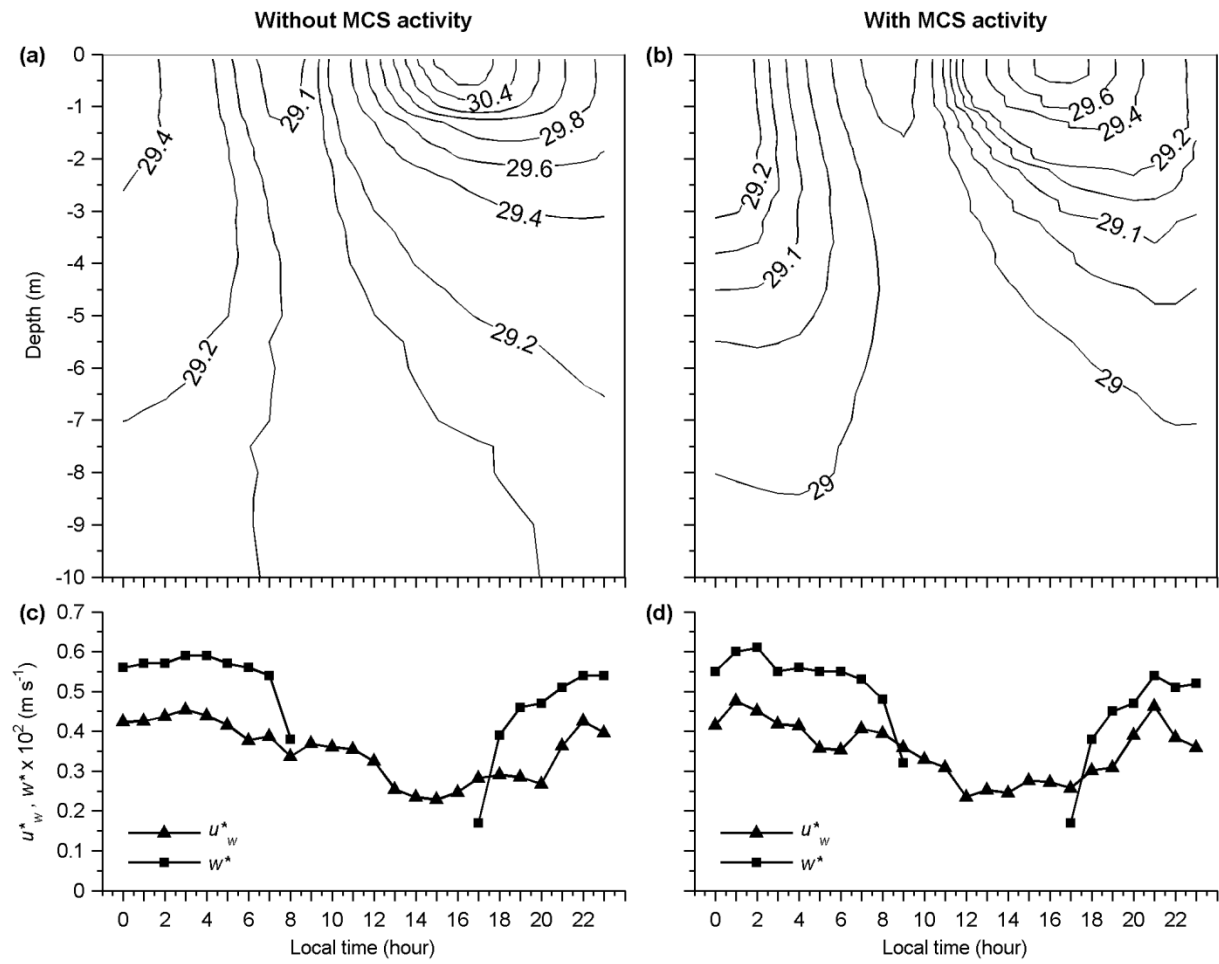


Figure 10.